SEARCH FOR ANOMALOUS TRILINEAR COUPLINGS OF ELECTROWEAK GAUGE BOSONS USING ANGULAR VARIABLES AT $\sqrt{s} = 13$ TeV AT CMS

by

KEVIN SIEHL

DISSERTATION

Submitted to the Graduate School

of Wayne State University,

Detroit, Michigan

in partial fulfillment of the requirements

for the degree of

DOCTOR OF PHILOSOPHY

2020

MAJOR: Physics

Approved By:

_____

Advisor Date

_____

_____

_____

DEDICATION

This thesis is dedicated to everyone who loves science, but didn't get the opportunity to study what they loved.

ACKNOWLEDGMENTS

I would like to acknowledge my parents for their continued support, without which, this would not have been possible.

$\sim$ *Kevin Siehl*

TABLE OF CONTENTS

LIST OF FIGURES

CHAPTER 1 INTRODUCTION

1.1 Motivation

While the standard model of particle physics has been greatly successful at explaining observations made in particle physics experiments, there are indications that it is not complete. Questions that the standard model leaves unanswered include why there are three generations of particles, why the particles have the masses that they do, and how does gravity fit into the picture. Observations that indicate that the standard model is incomplete include the apparent existence of dark matter, the discovery of neutrino oscillations, and the possible existence of sterile neutrinos [1].

Neutrino oscillations refer to the tendency of neutrinos to change identity to other types of neutrino as they travel through space. Sterile neutrinos are a possible fourth flavor of neutrino that, unlike the three known flavors, does not couple to ordinary matter. Dark matter is the hypothetical matter that contains the extra mass beyond that accounted for by visible matter, which is needed to explain the gravitational behavior of galaxies. Despite the unexplained observations, the vast majority of observations agree well with the standard model, leading us to pursue measurements that test the standard model at levels not previously explored, looking for signs of new physics.

1.2 Approach

There are generally two approaches to looking for physics beyond the standard model (BSM). The "top-down" approach is to start with a specific BSM theory, with specific predictions, such as new particles, and search for predictions of the theory. The "bottom up" approach is to look for deviations from the standard model and parameterize them in a model-independent way, such as by adding new terms in a generic way to the standard model Lagrangian. Such deviations will either be found, or there will be limits placed on how large they can be. In either case, constraints will be placed on what BSM theories could be consistent with Nature.

This work follows the bottom-up approach, searching for deviations in the couplings of

the electroweak gauge bosons to each other. Electroweak gauge bosons couple not only to fermions, but to one another as well. Such couplings determine the cross section with which the three types of electroweak gauge bosons interact with each other, and are included in the standard model Lagrangian. Because the standard model gives an exact prescription for these couplings, measuring the cross section of the interactions is one tool for probing its limits. There are terms that can be added to the standard model Lagrangian which affect these couplings, and also have an effect on the helicities of the gauge bosons, as discussed in Section 2.4. The helicities could potentially affect the angular distribution of the decay products. Angular distributions are therefore also investigated in this work as a possible means of placing more stringent limits on anomalous couplings.

The Large Hadron Collider (LHC) is able to collide particles at energies higher than any previous machine, giving potential for discovery. Deviations from standard model couplings, if they exist, are suppressed at the energies that have been probed so far. Therefore, looking at higher energies is one path to search for discovery. This study uses 2016 data produced at the Compact Muon Solenoid (CMS) detector at the LHC collider in Geneva, Switzerland.

CHAPTER 2 THEORY

2.1 The Standard Model

The standard model of particle physics is the most complete model we have of nature at the subatomic level, containing all the fundamental particles observed and all of the interactions except gravity. The particle content of the standard model is shown in Figure 2.1, with the particles separated first according to their intrinsic angular momentum, or spin, in units of Plank's fundamental constant, $\hbar$. (In particle physics, units are used in which $\hbar$; the speed of light, c; and the proton charge, e are equal to unity.) The particles in Figure 2.1 are color coded according to their spin. The particles with integral spin — unity for the gauge bosons and zero for the Higgs boson – obey Bose-Einstein statistics, which allows many of them to occupy the same state in a bound system. The particles with half integral spin obey Fermi-Dirac statistics, which does not allow more than one of them to occupy the same state in a bound system. This leads to the famous Pauli Exclusion Principle [2], and to the behavior of chemistry as we know it. The color of the spin half particles is further subdivided according to whether or not they participate in the strong interaction, explained below.

Particles that carry half integer spin are called fermions, and include the constituents of matter. Leptons are fermions that don't participate in the strong interaction, and can be further divided into charged leptons and neutrinos. Quarks – fermions that participate in the strong interaction – can be divided into up-type, with an electric charge of $\frac{2}{3}$ of the fundamental unit of charge, and down-type, with $-\frac{1}{3}$ of the fundamental electric charge. Particles with unit integral spin are known as gauge bosons, and they act as force carriers in the standard model. The only fundamental particle in the standard model with no spin, the Higgs boson, is responsible for giving mass to all massive particles in the standard model, including itself.

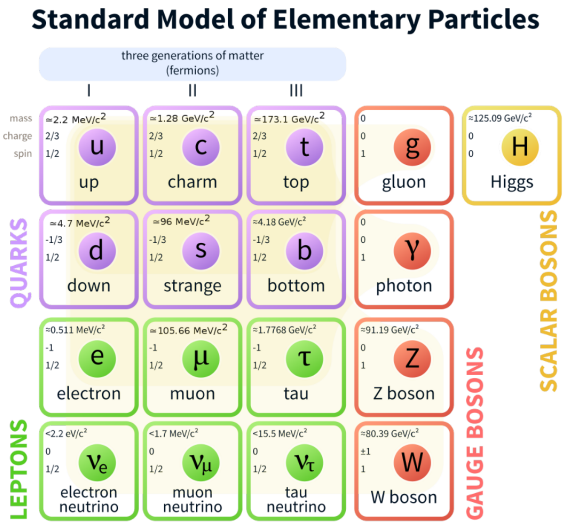

Figure 2.1: The periodic table of elementary particles in the standard model. Particles are colored according to their spin. Fermions are colored further according to whether they participate in the strong interaction. [3]

2.1.1 QCD

Quantum Chromodynamics (QCD) is the study of the strong interaction, which affects quarks, and is mediated by gluons. In addition to being carriers of the strong interaction, gluons also participate in it, complicating things. Gluons, like photons, are massless, so the strength of the force should in principle decrease as $1/r^2$, where r is the distance between interacting particles. However, because gluons participate in the interaction that they mediate, the strength of the interaction increases with distance. This causes a phenomenon known as asymptotic freedom [4], whereby quarks are only able to exist as free particles at extremely short distances from one another, or at very high energies. If quarks are separated from one another, more quark-antiquark pairs will form out of the vacuum, binding up the free quarks. Therefore, quarks are only observed as bound states.

There are three types of color charge that quarks come in, labelled red, green, and blue, and three corresponding anticolors for their antiparticles. Therefore, colorless bound states consist of either three quarks (baryons), three antiquarks (antibaryons), a quark and an antiquark (mesons), or, as was recently discovered, some combination of these [5].

2.1.2 Electromagnetism and the Nuclear Weak Interaction

The interaction mediated by the electrically charged W bosons is known as the charged current weak interaction, while the interaction mediated by the Z bosons is the neutral current weak interaction. Both of these mediating particles have mass, which limits the range of their interactions. The electromagnetic interaction is mediated by the massless photon, and has an infinite range, decreasing as $1/r^2$, where r is the distance between particles. While the photon and the Z boson have no charge, and do not participate in the forces that they mediate, the W boson has an electric charge, as well as a "Z charge" and a "W charge", meaning a coupling to the photon, the Z boson, and itself. The W's coupling to itself would lead charged weak interactions to have the same asymptotic behavior as the strong interaction; however, because W bosons have mass, the range of the interaction is restricted. Interactions mediated by massive particles have limited effective range, due to the fact that their potential falls off more rapidly than $1/r^2$.

2.2 Symmetries

Some of the guiding principles for particle physics have come from observing symmetries in Nature [2]. A symmetry involves changing a quantity and observing that the laws of Nature are the same before and after the change. There are generally two kinds of symmetries: continuous and discrete.

Continuous symmetries involve changing a quantity that can be varied continuously. They include rotational invariance, spatial-translation invariance, and time-translation invariance. Rotational invariance refers to the fact that Nature has no preferred orientation in space; spatial-translation invariance refers to the fact that Nature has no preference as far as the origin of one's coordinate system, and time-translation invariance refers to the fact that Nature has no preference to the origin of one's time scale. Other important continuous symmetries are the principle of relativity, which refers to Nature's indifference to the motion of an observer; and gauge invariance, which involves Nature's indifference to the zero point of potential energy.

Discrete symmetries involve changing a quantity that cannot be continuously varied. There are three important discrete symmetries in particle physics. First, there is parity, or spatial inversion. This involves changing the sign of all spatial coordinates and leaving the time coordinate unchanged, creating the equivalent of a mirror image process. Parity invariance, or P invariance, indicates that an interaction occurs at the same rate as its mirror image. A parity transformation on a particle's wave function is

$$\psi(x, y, z, t) \rightarrow P \cdot \psi(-x, -y, -z, t), \tag{2.1}$$

where P is the intrinsic parity of the system. Performing parity twice must return a system to its original state, because the mirror image of the mirror image is the original system. Therefore P, if well-defined, can only take the values of ± 1. Next, charge conjugation parity, or C-parity, involves exchanging every particle with its antiparticle. An interaction is C invariant if it occurs at the same rate as an identical interaction with antiparticles in place of particles. The operation of charge conjugation is given by

$$\psi(x, y, z, t) \rightarrow C \cdot \overline{\psi}(x, y, z, t), \tag{2.2}$$

where $\overline{\psi}$ represents the antiparticle of ψ. Here, C is the intrinsic C-parity of the system, and if well-defined, can only take the values of ± 1, because performing a C-parity operation twice must return the original state; the antiparticle of an antiparticle is the original particle. Finally, there is time reversal invariance, or T invariance. This involves inverting the sign of the time coordinate while leaving the spatial coordinates unchanged. An interaction is T invariant if it occurs at the same rate as its backward-in-time counterpart. A time reversal transformation of a system is given by

$$\psi(x, y, z, t) \rightarrow \psi^*(x, y, z, -t), \tag{2.3}$$

where ψ^* represents the complex conjugate of ψ. Unlike the other two discrete symmetries, time reversal does not correspond to any intrinsic quantity to conserve; there is no intrinsic T-parity of a system. This is the reason for the lack of an overall T-factor outside the transformed wave function. For discrete symmetries, only linear operators correspond to conserved quantities [2], and without a conservation law to test it, an intrinsic T-factor is fundamentally unmeasurable, and therefore meaningless. The complex conjugation means that the time reversal operator is an antilinear rather than a linear operator. Performing time reversal twice will give back the original system, as with the other two discrete symmetries.

2.3 Electroweak Symmetry Breaking

The standard model Lagrangian for the electroweak interaction is based on $SU(2)_L \times U(1)_Y$ symmetry [6]. Before being broken by the Higgs mechanism, the Lagrangian for trilinear gauge couplings is

$$\mathcal{L} = -\frac{1}{4}\vec{W}^{\mu\nu} \cdot \vec{W}_{\mu\nu} - \frac{1}{4}B^{\mu\nu}B_{\mu\nu} - g\vec{W}_\mu \times \vec{W}_\nu, \tag{2.4}$$

where g is a coupling constant. There are three W fields represented by the vector $\vec{W} = (W_1, W_2, W_3)$, and a B field.

The double index tensor is defined as

$$X_{\mu\nu} = \partial_\mu X_\nu - \partial_\nu X_\mu. \tag{2.5}$$

With a change of coordinates, the terms can be rearranged. Four new fields can be defined: A, Z, and $W^\pm$; defined as

$$A = W_3 \sin\theta_W + B\cos\theta_W, \tag{2.6a}$$

$$Z = W_3 \cos\theta_W - B\sin\theta_W, \tag{2.6b}$$

and

$$W_{\pm} = \frac{1}{\sqrt{2}}(W_1 \mp iW_2). \tag{2.6c}$$

Then, the Lagrangian is

$$\mathcal{L} = -\frac{1}{4}A^{\mu\nu}A_{\mu\nu} - \frac{1}{4}Z^{\mu\nu}Z_{\mu\nu} - \frac{1}{2}W_{+}^{\mu\nu}W_{\mu\nu}^{-} + \mathcal{O}(g) + \mathcal{O}(g^2), \tag{2.7}$$

where A is the photon field, Z is the neutral weak boson field, and $W^{\pm}$ are the charged weak boson fields. The $\mathcal{O}(g)$ term represents the trilinear gauge couplings that this work is based on, while the $\mathcal{O}(g^2)$ term represents quartic couplings. The $\mathcal{O}(g)$ term expands to give

$$\mathcal{L}_{WWW3} = ig\left((W_{\mu\nu}^{-}W_{+}^{\mu} - W_{-}^{\mu}W_{\mu\nu}^{+})W_3^{\nu} + W_{\mu}^{-}W_{\nu}^{+}W_3^{\mu\nu}\right). \tag{2.8}$$

Expanding W_3 into A and Z and defining $e = g\sin\theta_W$, Equation 2.8 becomes

$$\mathcal{L}_{WWW3} = \mathcal{L}_{WWZ}^{\mathrm{SM}} + \mathcal{L}_{WW\gamma}^{\mathrm{SM}}, \tag{2.9}$$

with $\mathcal{L}_{WWZ}$ and $\mathcal{L}_{WW\gamma}$ represented by the equation

$$\mathcal{L}_{WWV}^{\mathrm{SM}} = ig_{WWV}\left((W_{\mu\nu}^{\dagger}W^{\mu} - W^{\dagger\mu}W_{\mu\nu})V^{\nu} + W_{\mu}^{\dagger}W_{\nu}V^{\mu\nu}\right). \tag{2.10}$$

In Equation 2.10, $W^{\dagger}$ has been used in place of W^{-} and W has been used in place of W^{+}. Here, V represents either the photon field A, or the Z field. The constant ig_{WWV} represents e in the photon case and $e\cot\theta_W$ in the Z case. Equation 2.10 represents the vertex highlighted in Figure 2.2, showing the trilinear interaction of the W field to that of the Z field or the electromagnetic (photon) field. There are also quartic couplings of the fields, shown in Figures 2.3 and 2.4, which are not studied in this work.

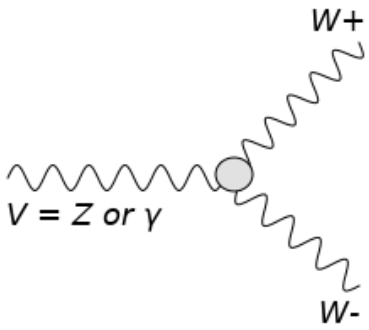

Figure 2.2: The trilinear couplings of the electroweak gauge bosons. This thesis is based on searching for deviations in this coupling from the standard model prediction.

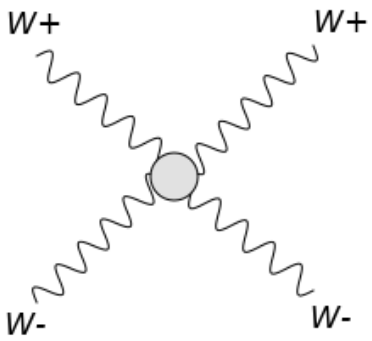

Figure 2.3: Standard model electroweak quartic gauge coupling with four Ws.

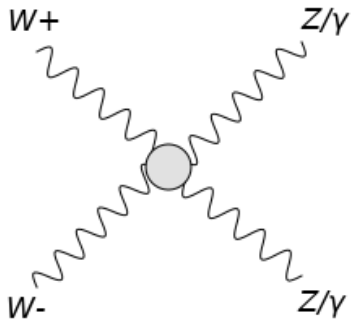

Figure 2.4: Standard model electroweak quartic gauge couplings with Ws and neutral bosons.

2.4 Anomalous Couplings

Electroweak gauge bosons couple to each other as well as to fermions. In the standard model, at tree level, there are two trilinear gauge couplings; WWZ and $WW\gamma$. The result of Equation 2.10 completely determines these couplings. Assuming only Lorentz invariance [7], a more general Lagrangian can be written:

$$\begin{aligned}\mathcal{L}_{WWV} &= ig_{WWV}\Big(g_1^V(W^\dagger_{\mu\nu}W^\mu - W^{\dagger\mu}W_{\mu\nu})V^\nu + \kappa_V W^\dagger_\mu W_\nu V^{\mu\nu} + \frac{\lambda_V}{M_W^2}W^{\dagger\nu}_\mu W^\rho_\nu V^\mu_\rho + \\ &+ ig_4^V W^\dagger_\mu W_\nu(\partial^\mu V^\nu + \partial^\nu V^\mu) - ig_5^V\epsilon^{\mu\nu\rho\sigma}(W^\dagger_\mu\partial_\rho W_\nu - \partial_\rho W^\dagger_\mu W_\nu)V_\sigma + \\ &+ \widetilde{\kappa}_V W^\dagger_\mu W_\nu \widetilde{V}^{\mu\nu} + \frac{\widetilde{\lambda}_V}{M_W^2}W^{\dagger\nu}_\mu W^\rho_\nu \widetilde{V}^\mu_\rho\Big),\end{aligned} \tag{2.11}$$

where the terms in color are the parameters under consideration. Those colored blue are 1 in the standard model while those colored red are 0 in the standard model. The term $\widetilde{X}^{\mu\nu}$ is shorthand for $\frac{1}{2}\epsilon^{\mu\nu\rho\sigma}X_{\rho\sigma}$ [7]. The following quantities are defined for convenience:

$$\Delta\kappa_\gamma = \kappa_\gamma - 1, \tag{2.12a}$$

$$\Delta\kappa_Z = \kappa_Z - 1, \tag{2.12b}$$

$$\Delta g_1^Z = g_1^Z - 1, \text{ and} \tag{2.12c}$$

$$\Delta g_1^\gamma = g_1^\gamma - 1. \tag{2.12d}$$

Equation 2.11 contains seven independent parameters for each vertex, giving a total of fourteen altogether. This number can be narrowed down by making additional assumptions. Requiring electromagnetic gauge invariance forces $g_1^\gamma = 1$ and $g_4^\gamma = g_5^\gamma = 0$ in Equation 2.11. This reduces the number of independent anomalous parameters to eleven. If $SU(2)\otimes U(1)$ gauge symmetry is also included [7], more terms can be eliminated, using the following relations:

$$\lambda_Z = \lambda_\gamma = \lambda, \tag{2.13a}$$

$$\widetilde{\lambda}_Z = \widetilde{\lambda}_\gamma = \widetilde{\lambda}, \tag{2.13b}$$

$$\Delta\kappa_Z = \Delta g_1^Z - \Delta\kappa_\gamma \tan^2\theta_W, \tag{2.13c}$$

$$\widetilde{\kappa}_Z = -\widetilde{\kappa}_\gamma \tan^2\theta_W, \text{ and} \tag{2.13d}$$

$$g_4^Z = g_5^Z = 0. \tag{2.13e}$$

This reduces the number of independent anomalous parameters to five. Three of them, Δg_1^Z, $\Delta\kappa_\gamma$, and λ, conserve both parity and charge conjugation parity, while the other two, $\widetilde{\kappa}_\gamma$ and $\widetilde{\lambda}$ violate either parity or C-parity.

If the anomalous parameters are assumed constant with respect to the center-of-mass energy, the Lagrangian will give results violating unitarity at sufficiently high energies [7]. For this reason, form factors are sometimes used to preserve unitarity. The anomalous couplings then take the following form:

$$\Delta g_1^Z \longrightarrow \frac{\Delta g_1^Z}{\left(1 + \dfrac{s}{\Lambda_{FF}^2}\right)^n}, \tag{2.14a}$$

$$\Delta\kappa_\gamma \longrightarrow \frac{\Delta\kappa_\gamma}{\left(1 + \dfrac{s}{\Lambda_{FF}^2}\right)^n}, \tag{2.14b}$$

$$\lambda \longrightarrow \frac{\lambda}{\left(1 + \dfrac{s}{\Lambda_{FF}^2}\right)^n}, \tag{2.14c}$$

$$\widetilde{\kappa}_\gamma \longrightarrow \frac{\widetilde{\kappa}_\gamma}{\left(1 + \dfrac{s}{\Lambda_{FF}^2}\right)^n}, \tag{2.14d}$$

$$\widetilde{\lambda} \longrightarrow \frac{\widetilde{\lambda}}{\left(1 + \frac{s}{\Lambda_{FF}^2}\right)^n}. \tag{2.14e}$$

Here, s is the square of the center of mass energy, Λ_{FF} is the energy cutoff scale of the form factor, and n is an integer.

The current practice of the CMS collaboration is to assume that Λ_{FF} is infinite, or equivalently, that the value of n is 0. Constraints already placed on the anomalous parameters put them well within unitarity bounds at present collider energies. If non-zero values exist for any of these parameters, and are measured at present energies, other operators may come into play at higher energies to "rescue" unitarity.

Another way of expressing the anomalous parameters, is through effective field theory operators [7]. This involves writing the Lagrangian as the standard model Lagrangian with higher order operators appended to it. Including operators of dimension six or below, this gives

$$\mathcal{L} = \mathcal{L}_{\text{SM}} + \frac{c_{WWW}}{\Lambda^2}\mathcal{O}_{WWW} + \frac{c_W}{\Lambda^2}\mathcal{O}_W + \frac{c_B}{\Lambda^2}\mathcal{O}_B + \frac{\widetilde{c}_{WWW}}{\Lambda^2}\widetilde{\mathcal{O}}_{WWW} + \frac{\widetilde{c}_W}{\Lambda^2}\widetilde{\mathcal{O}}_W. \tag{2.15}$$

The operators in Equation 2.15 are defined as,

$$\mathcal{O}_{WWW} = \text{Tr}[\hat{W}_{\mu\nu}\hat{W}^{\nu\rho}\hat{W}_{\rho}^{\mu}], \tag{2.16a}$$

$$\mathcal{O}_W = (D_\mu\Phi)^\dagger \hat{W}^{\mu\nu}(D_\nu\Phi), \tag{2.16b}$$

$$\mathcal{O}_B = (D_\mu\Phi)^\dagger \hat{B}^{\mu\nu}(D_\nu\Phi), \tag{2.16c}$$

$$\widetilde{\mathcal{O}}_{WWW} = \text{Tr}[\widehat{\widetilde{W}}_{\mu\nu}\hat{W}^{\nu\rho}\hat{W}_{\rho}^{\mu}], \tag{2.16d}$$

$$\widetilde{\mathcal{O}}_W = (D_\mu\Phi)^\dagger \widehat{\widetilde{W}}^{\mu\nu}(D_\nu\Phi). \tag{2.16e}$$

Here, Φ is the Higgs field, and the operators in Equation 2.16 are defined as follows:

$$D_\mu = \partial_\mu + i\frac{g}{2}\sigma_i W_\mu^i + \frac{g'}{2}B_\mu, \tag{2.17a}$$

$$\hat{W}_{\mu\nu} = i\frac{g}{2}\sigma_i \left(W_{\mu\nu}^i + g\epsilon_{ijk}W_\mu^j W_\nu^k\right), \tag{2.17b}$$

$$\hat{B}_{\mu\nu} = i\frac{g'}{2}B_{\mu\nu}, \text{ and} \tag{2.17c}$$

$$\widehat{\widetilde{W}}_{\mu\nu} = \frac{1}{2}\epsilon^{\mu\nu\rho\sigma}\hat{W}_{\rho\sigma}. \tag{2.17d}$$

Here, $g' = g\tan\theta_W$ and σ^i are the Pauli spin matrices. The effective field theory coefficients; c_W, c_{WWW}, $\widetilde{c}_B$, $\widetilde{c}_W$, and c_B; are always expressed divided by a factor of Λ^2, which represents an energy scale of new physics. The actual parameters of interest therefore are the ratios of of the coefficients with the energy scale. Neither the coefficients nor the energy scale have any existence independent of the other.

The translations between the effective field theory coefficients and the traditional parameters are as follows:

$$\frac{c_W}{\Lambda^2} = \frac{2}{m_Z^2}\Delta g_1^Z, \tag{2.18a}$$

$$\frac{c_{WWW}}{\Lambda^2} = \frac{\sqrt{2}}{12G_F m_W^4}\lambda, \tag{2.18b}$$

$$\frac{\widetilde{c}_W}{\Lambda^2} = \frac{2}{m_W^2}\widetilde{\kappa}_\gamma = -\frac{2}{m_W^2}\frac{1}{\tan^2\theta_W}\widetilde{\kappa}_Z, \tag{2.18c}$$

$$\frac{\widetilde{c}_{WWW}}{\Lambda^2} = \frac{\sqrt{2}}{12G_F m_W^4}\widetilde{\lambda}, \text{ and} \tag{2.18d}$$

$$\frac{c_B}{\Lambda^2} = \frac{2}{m_W^2}\Delta\kappa_\gamma - \frac{2}{m_Z^2}\Delta g_1^Z = \frac{1}{\tan^2\theta_W}\left(\frac{2}{m_Z^2}\Delta g_1^Z - \frac{2}{m_W^2}\Delta\kappa_Z\right). \tag{2.18e}$$

2.4.1 Present Analysis

This analysis studies events where two incoming partons form an electroweak gauge boson, which then decays into two more gauge bosons, as shown in Figure 4.1. This results in either a pair of Ws or a W and a neutral gauge boson. For the latter case, only events where the neutral particle is a Z boson are considered. The final state is a 'boosted' jet along with a lepton and missing energy. The events in this study involve gauge bosons of sufficiently high energy that when they decay hadronically, the two jets are reconstructed as a single 'fat' or 'boosted' jet by the jet reconstruction algorithm. The two jets are back to back in the gauge boson's rest frame, due to conservation of momentum. Boosting from the gauge boson's rest frame to the lab frame, these jets tend to be closer together the higher the boson's momentum. Because this analysis selects leptons with high p_T, this leads to hadronic gauge bosons with high momentum as well. When the final state is a pair of W bosons, the couplings involve a mixture of WWZ and $WW\gamma$ vertices, because the intermediate neutral gauge boson is a linear combination of the photon and Z boson. However, when the final state is a W and a Z boson, the second vertex is not involved.

CHAPTER 3 EXPERIMENTAL SETUP

The analysis uses 2016 data collected at the Large Hadron Collider (LHC), with the Compact Muon Solenoid (CMS) detector, in Geneva, Switzerland. The accelerator facility used to generate the proton–proton collisions is described in Section 3.1 and the relevant aspects of the CMS detector are discussed in Section 3.2.

3.1 Large Hadron Collider

The LHC [8, 9] is a particle accelerator (Figure 3.1) located underground, beneath the border of Switzerland and France, northwest of Geneva, Switzerland (Figure 3.2). Construction of the LHC was approved by the European Council for Nuclear Research (CERN) in 1990. The LHC was built to search for the Higgs boson, found in 2012, as well as to search for possible constituents of dark matter or proposed extensions of the standard model. The LHC is a circular proton-proton superconducting synchrotron, 27 km in circumference. Counter circulating beams of protons collide at four locations corresponding to the four major experiments. The energy available for the collision is proportional to the incident beam energy.

Protons, being more massive than electrons, lose less energy to synchrotron radiation from their centripetal acceleration, allowing for higher energies to be achieved. The disadvantage of protons is that, unlike electrons, they are composite objects. This means that the collisions are between partons (quarks and gluons) within the proton, with a fraction of the proton's momentum that is not known. The LHC's design called for a 14 TeV center-of-mass energy. It ran at a center-of-mass energy of 7 TeV in 2010 and 2011, and its energy was increased to 8 TeV in 2012. It was shut down for about two years in 2013 and 2014, and restarted at the end of 2015 with its current center-of-mass energy of 13 TeV.

The process of producing beams of protons begins with extracting protons from molecules of hydrogen gas. A quantity of H_2 gas is ionized, yielding H^- and H^+ ions that are separated in an electric field. The H^+ ions (protons) are separated into bunches that begin the acceleration process [11]. Proton beams are first accelerated by a linear accelerator (LINAC 2), to about 50 MeV, then enter the Proton Synchrotron Booster (PSB), which accelerates

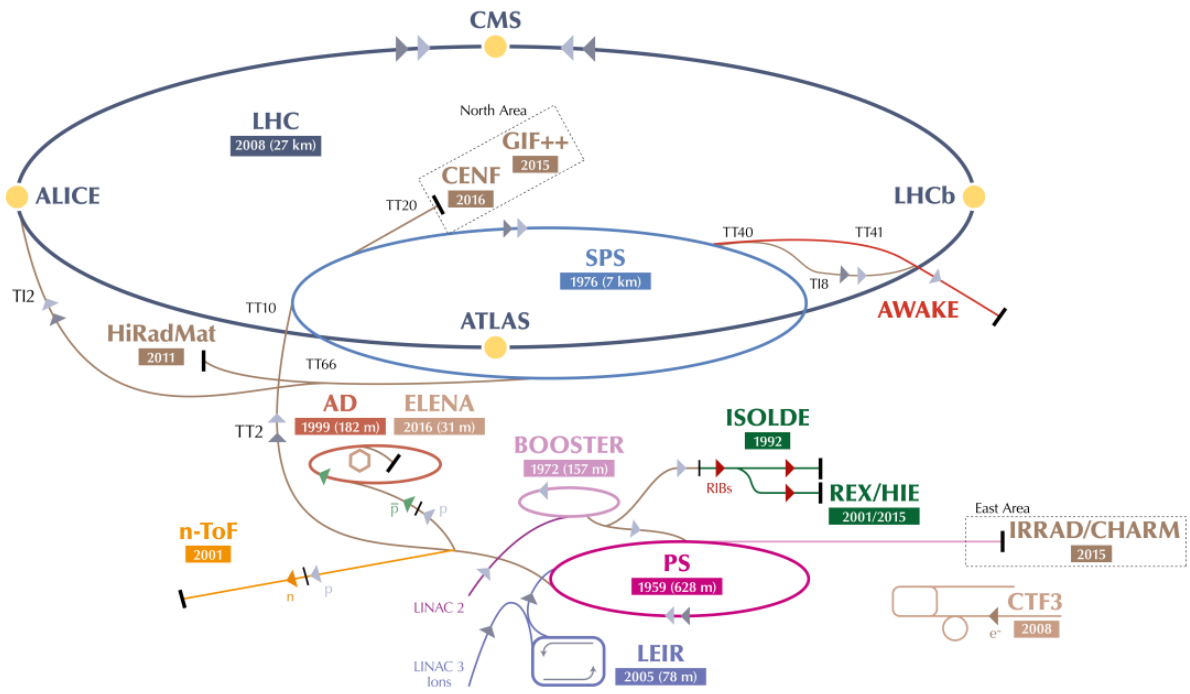

Figure 3.1: Accelerator infrastructure at CERN, showing interconnection of machines and transfer of particles between them. [10].

them further to 1.4 GeV [11]. They're then fed into the Proton Synchrotron to be accelerated up to 26 GeV and then to the Super Proton Synchrotron to accelerate them further to 450 GeV [11]. They are then fed into the LHC, in two beams, going in opposite directions. The protons are fed in bunches, around 1.15×10^{11} protons in a bunch [8]. There are 2808 bunches per ring, spaced about 25 ns apart [11]. When all the bunches have been injected into the LHC at 450 GeV, acceleration of the protons begins. This is called a fill. After about 20 minutes, they reach their final energy of 6.5 TeV.

3.1.1 Luminosity

The number of times a given type of process occurs depends on the process's cross section, σ, multiplied by the collider's integrated luminosity:

$$N = \mathcal{L} \times \sigma, \tag{3.1}$$

Figure 3.2: The LHC has a circumference of 27 km, and lies underground, spanning two countries. [12]

where the integrated luminosity is the instantaneous luminosity integrated over time, $\mathcal{L} = \int L \, \mathrm{d}t$.

The instantaneous luminosity, with units of inverse area per time, is given by [11]

$$L = \frac{\gamma \nu N_B N_p^2}{4\pi \epsilon_n \beta^*} F, \tag{3.2}$$

where γ is the Lorentz factor of the protons (6929 for a proton energy of 6.5 TeV), ν is the frequency of collisions (40 kHz for 25 ns spacing), N_B is the number of bunches (2808 as stated above), N_p is the number of protons in a bunch (1.15×10^{11} as stated above), ϵ_n is the normalized transverse emittance, β^* is the betatron function, and F is a dimensionless geometrical reduction factor accounting for the beams' crossing angle. With a betatron function of about 0.55 m, an emittance of 3.75 μm, and a geometrical reduction factor of 0.836 [8], this works out to a luminosity of roughly 3×10^{34} cm^{-2}sec^{-1}.

3.2 The CMS Detector

The CMS detector is one of four main detectors at the LHC. It is located underground, in the French village of Cessy, north of the main CERN facilities. It is located at one of the four interaction regions of the LHC where the beams of particles are brought into collision.

The CMS detector is built around – and within – a superconducting solenoid with an internal diameter of 6 m (Figure 3.3), producing a solenoidal magnetic field of 3.8 T. The

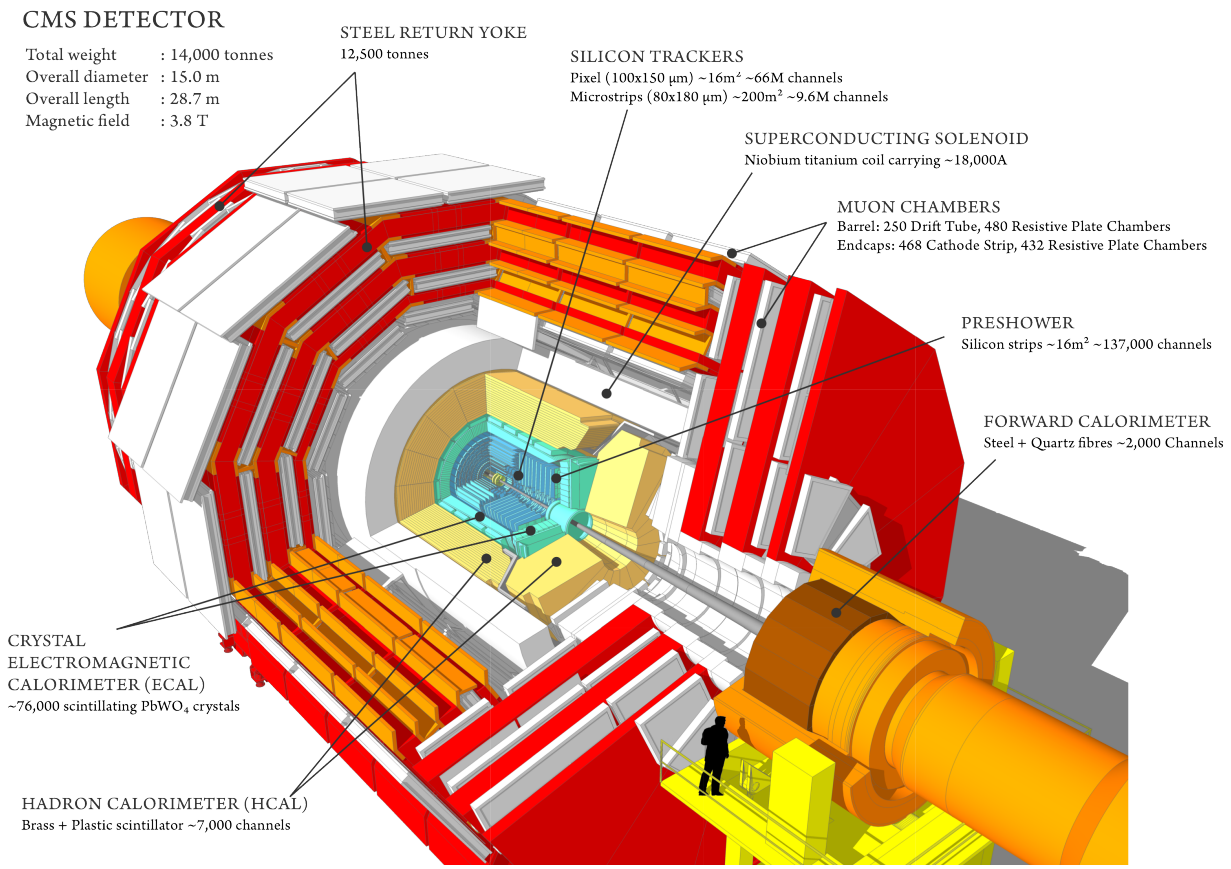

Figure 3.3: Overview of the CMS detector with its multiple subsystems. [13]

CMS solenoid has the highest stored energy of any magnet to date. The detector is built in concentric cylinders, each system nesting inside the others, like Russian nesting dolls. The innermost region of the detector is the silicon tracker. This measures the tracks of charged particles, out to a radius of 1.1 meters. Outside the silicon tracker is the electromagnetic calorimeter (ECAL) which measures energy deposits from electrons and photons. Further outside is the hadronic calorimeter (HCAL), which measures energy from hadrons that come out of the collisions. Outside of the ECAL and HCAL is the superconducting solenoid already mentioned. Outside the solenoid is the muon system. Muons are typically the only particles to make it out this far, so a special system for measuring them is located outside the other systems. The muon system is interleaved with the return yoke of the solenoid.

3.2.1 Solenoid Magnet

The solenoid magnet encloses all of the detector subsystems except for the muon tracking system and has an inner diameter of 6 m, and is 12.5 m in length. A nearly constant 3.8 T magnetic field exists inside the solenoid. Outside the solenoid is a steel return yoke, fully saturated to about 2 T. The magnetic field is crucial to measurements of particle momentum. The well-known Lorentz force law,

$$\mathbf{F} = q\mathbf{v} \times \mathbf{B}, \tag{3.3}$$

when applied to a magnetic field solely in the z-direction ($\mathbf{B} = B\hat{z}$), and combined with the centripetal force equation,

$$\mathbf{F}_c = \gamma^2 \frac{mv^2}{R^2}, \tag{3.4}$$

leads to a relation between radius and transverse momentum. This equation,

$$R = \gamma \frac{p_T}{|q|B}, \tag{3.5}$$

is used to compute the transverse momentum of particles, if the absolute value of their charge is known. The sign of the charge can be inferred from the direction of the curvature.

3.2.2 Silicon Tracker

The silicon tracker in CMS contains semiconductor tracking devices [14]. It is the innermost part of the detector, inside the solenoid, as shown in Figure 3.4, with a length of 5.8 m and a cylindrical diameter of 2.5 m. The innermost part consists of silicon pixels, while silicon strips are used further out. Silicon diodes produce currents when charged particles pass through them. Particles pass through more than one layer, allowing the tracks of charged particles to be inferred. The tracks are then used to calculate both the position and the momentum of the particle. This is necessary to determine the origin of a particle (decay product, from primary interaction point). The silicon tracker has an area of 200 m^2 of silicon sensors. The dimensions are designed to keep the particle flux per collision low.

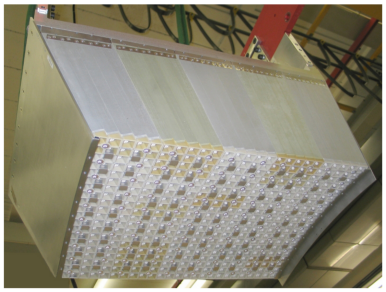

Figure 3.4: The front view of a module forming part of the Silicon Tracker. [15]

The pixel detector barrel has three layers, located 4.4, 7.3, and 10.2 cm from the beam. The innermost layer has a hit rate density of around 1 MHz/mm^2. With 100 by 150 μm pixels, this gives an occupancy on the order of 10^{-4} hits per sensor per bunch crossing. Further out, with a reduced flux, silicon strip detectors are used, 10-25 cm in length and 80-180 μm in width.

3.2.3 Electromagnetic Calorimeter

The electromagnetic calorimeter (ECAL) is designed to measure the energy of electrons and photons [16, 17]. Because electrons and photons interact with the solenoid material, the ECAL is positioned inside the solenoid, to measure the particles before they encounter the material. This creates a need for compactness. It is made of lead tungstate ($PbWO_4$) crystals. When particles collide with the crystals, light is produced with an intensity proportional to the energy of the particles. Photodetectors then collect the light. Lead tungstate was chosen in part due to its short radiation length of 0.89 cm. The radiation length is the average length that electrons will travel in the material before their energy is $1/e$, or around 37%, of their original energy, where e is the base of natural logarithms. Lead tungstate has a Molière radius of about 2.2 cm. The Molière radius is the radius at which 90% of the electromagnetic showering is contained. The small Molière radius was another reason for the choice of lead tungstate. Another property of lead tungstate that makes it desirable is the short scintillation decay time of the crystals – the delay between absorbing energy and emitting light – of around 25 ns for 80% of the energy to be emitted as light. The

barrel portion of the ECAL has a pseudorapidity range of $|\eta| < 1.479$ and consists of 61,200 crystals, while the endcap portions cover the pseudorapidity range of $1.566 < |\eta| < 3.0$ and consist of 7,324 crystals each. Pseudorapidity is defined by the relation

$$\eta = -\ln\left(\tan\frac{\theta}{2}\right), \tag{3.6}$$

where θ is the polar angle from the beam line. The crystals have a cross section of 2.2 cm by 2.2 cm along the geometric line facing the interaction point. The gap in pseudorapidity is due to cabling and tracker support structure. The crystal thickness in the barrel (endcap) is 23 (22) cm, which corresponds to about 25.8 (24.7) radiation lengths. The energy resolution of the ECAL is given by [18]

$$\left(\frac{\delta_E}{E}\right)^2 = \left(\frac{S}{\sqrt{E}}\right)^2 + \left(\frac{N}{E}\right)^2 + C^2, \tag{3.7}$$

where S is a stochastic term and has a value of 0.028 $\text{GeV}^{\frac{1}{2}}$, N is a noise term, with a value of 0.12 GeV, and C is a constant term with a value of 0.30%.

3.2.4 Hadronic Calorimeter

The hadronic calorimeter (HCAL) is the part of the CMS detector that is designed to measure the energy of both charged and neutral hadrons [19, 20]. It lies just outside the ECAL. The HCAL consists of active material placed between brass absorber plates. It has a total coverage of $|\eta| < 5.0$. The active elements are 4 mm thick plastic scintillator tiles. The barrel has a coverage up to $|\eta| < 1.3$ and the endcaps cover $1.3 < |\eta| < 3.0$. The HCAL has a varying thickness, ranging from 5.82 to 10 nuclear interaction lengths. The nuclear interaction length is the mean free path of a particle before undergoing an inelastic hadronic collision. There is also a forward HCAL (HF) located close to the beam pipe, with a coverage of $3.0 < |\eta| < 5.0$. The HF encounters energy deposits five to ten times higher than the rest of the detector, and thus needs to be very radiation hard. It is constructed of quartz fiber Cherenkov detectors. These fibers are embedded in steel to induce electromagnetic and

hadronic showers. Measuring the development of showers is assisted by the fact that half of the quartz fibers extend the full length of the detector, while the other half start 22 cm away from the interaction point. The energy resolution for the HCAL can be given by Equation 3.7, with the stochastic term, S, having a value of 1.15 $\text{GeV}^{\frac{1}{2}}$, the constant term, C, having a value of 5.5%, and the noise term, N, being negligible.

3.2.5 Muon System

Muons, being heavier than electrons by a factor of around 200, are much less susceptible to radiative energy loss, and pass mostly through the ECAL and HCAL systems. The muon system is outside of the solenoid, and interleaved inside of a steel return yoke. This arrangement is designed to ensure that nearly all (well over 99%) of the particles that enter the muon system are muons. The muon system consists of three different subsystems using different types of gaseous detectors: drift tubes (barrel), cathode strip chambers (endcaps), and resistive plate chambers (barrel and endcaps). When electrically charged particles pass through a gas and ionize the gas molecules, the electric field will cause the ionized particles to drift toward the anode where a signal is read out.

Drift Tube System

The barrel portion of the muon detector, with a coverage in pseudorapidity of $|\eta| < 1.2$, is composed of drift tube (DT) chambers [21]. The DTs are rectangular aluminum tubes 2.4 m long, with a cross section of 13 mm by 42 mm. Each tube has a beryllium tungsten anode wire, 50 μm in diameter, and plated in gold. The interior of each DT contains aluminum strips to shape the electric field, shown in Figure 3.5. The gas inside the DTs is a mixture of 85% argon and 15% carbon dioxide. Passing charged particles ionize the gas and the electric field accelerates the electrons toward the anode wire, and a signal is sent in the form of an electrical pulse to the anode where a signal is read out. The wires in the outer DTs are parallel to the beam direction, while the inner DTs are perpendicular to the beam direction, providing a measure of the bending of muons in the magnetic field. There are

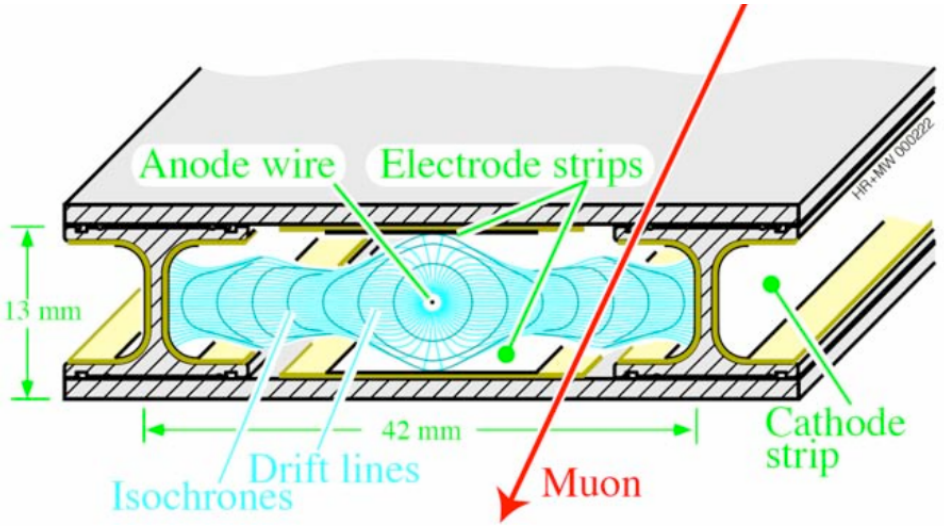

Figure 3.5: Cross section of a drift tube. The plates at the top and bottom of the cell are at ground potential. The potentials applied to the electrodes are +3600V for wires, +1800V for strips, and -1200V for cathodes. [15]

a total of around 172 thousand cells, giving a position resolution of around 100 μm and a timing resolution of a few nanoseconds.

Cathode Strip Chambers

The forward regions of the muon detector, with a pseudorapidity range of $0.9 < |\eta| < 2.4$, sits in a non-uniform magnetic field. The Cathode Strip Chamber (CSC) system is in this region [22]. CSCs are constructed of trapezoidal, multi-wire chambers, as shown in Figure 3.6. Each chamber contains six layers of cathode strip chambers, each filled with an Ar-CO_2-CF_4 gas mixture. Copper cathode strips span the radial direction at a constant Φ. Each layer has a plane of anode wires, 50 μm in diameter, running perpendicular to the strips and separated by varying distances ($\sim$3.5 mm). When a muon passes through a chamber, an avalanche of electrons is generated at nearby anode wires and a mirror pulse of positive ions in the cathode strips. The CSCs are arranged perpendicular to the beam direction, and give full coverage in Φ. The innermost station for each endcap is composed of three rings of CSCs in the radial direction, while other stations have two rings, as shown in Figure 3.7.

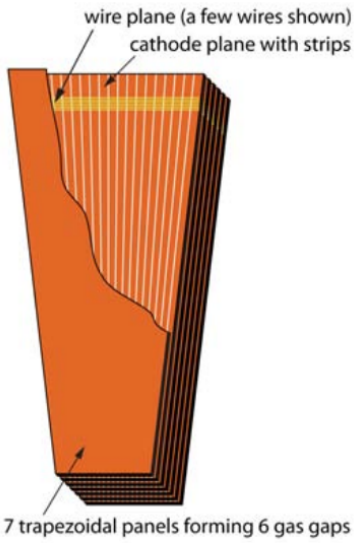

Figure 3.6: Layout of a CSC made of seven trapezoidal panels. The panels form six gas gaps with planes of sensitive anode wires. [15]

There are a total of 540 CSC chambers.

Resistive Plate Chambers

Resistive Plate Chambers (RPC), are located in both the barrel and endcap regions, and provide a fast trigger signal [23]. The RPCs are constructed from a thin layer of readout strips between electrodes, held at high electric potential, and are filled with $C_2H_2F_4$ gas. When a muon passes through, the sum of the signal between the two gaps is read out at the center plate. The plates are separated by 2 mm, ensuring that the charge is detected within 25ns, necessary to assign the muon to the correct bunch crossing. The RPCs are dispersed in six layers between the DTs in the barrel region, and in three layers between the CSCs in the endcap region.

3.2.6 Trigger and Data Acquisition

The LHC provides high interaction rates. For protons, the interval is 25 ns between collisions, giving a crossing frequency of 40 MHz [24, 25], or 40 million events per second. Because it is not currently possible to store and process such a large amount of data, a

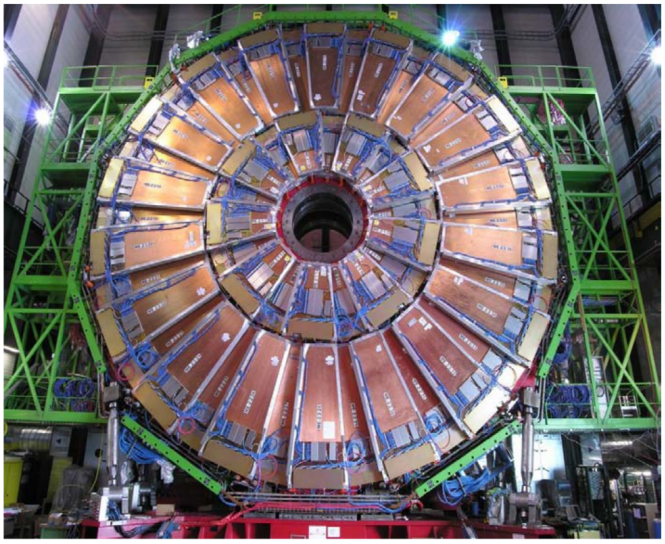

Figure 3.7: A photo of the CMS detector, showing ME4 of the CSCs. The outer ring here consists of 36 chambers and the inner ring contains 18 chambers. The chambers in the inner and outer rings overlap to give continuous coverage. [15]

reduction in rate has to be achieved. Only about 1000 events per second are actually recorded and stored. The trigger system [24] is designed for this task. There are two trigger steps: the first is the Level-1 (L1) Trigger and the second is the High-Level Trigger (HLT). The flow of data in the L1 Trigger is shown in Figure 3.8. The L1 trigger is a hardware system built from programmable electronics [26]. Data from the HCAL and ECAL are sent to a Global Calorimeter Trigger (GCT), while data from the muon systems are sent to a Global Muon Trigger (GMT). The GCT and GMT then send their data to a Global Trigger (GT), which makes a final decision as to whether or not to keep an event.

Initially, the L1 trigger system handles the muon and calorimeter system information independently. The energy and shapes of ECAL deposits contribute to photon and electron candidates, while HCAL energy deposits are used to identify clusters of hadrons. Particle candidates are sorted by p_T, and the total energy of the event is computed. This information is sent to the global trigger for a decision. The muon trigger system builds track candidates by matching hits in its three subsystems (CSC, RPC, and DT). Track finders in the barrel, endcap, and overlap region combine the track segments to form muon candidates. The

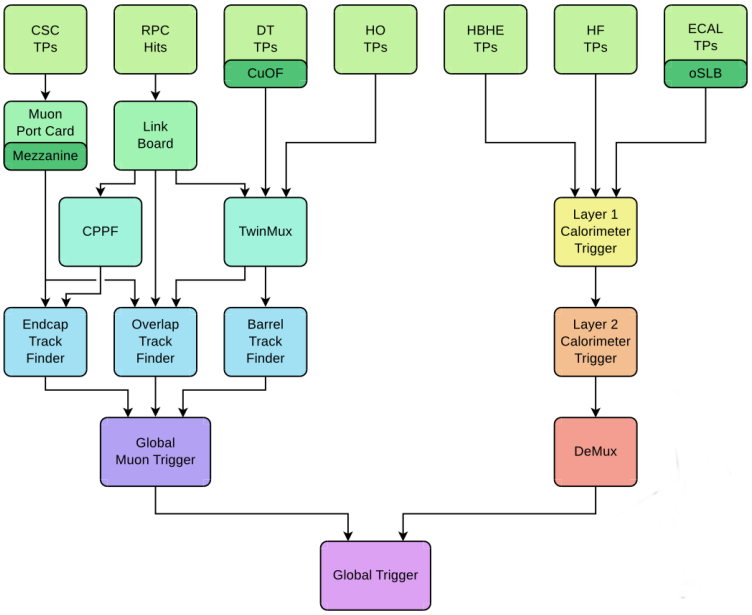

Figure 3.8: The L1 Trigger system [24] uses several components of the CMS detector for its operation. Triggers from the various muon systems send information to the Global Muon Trigger (GMT), while the Global Calorimeter Trigger (GCT) and the GMT send their information to the Global Trigger(GT).

muon candidates are sorted by p_T, then sent to the global trigger. The global trigger uses the information from the muon and calorimeter triggers to test physics objects and physics object combinations, based on built in kinematic criteria, before making a decision to accept or reject an event. The set of conditions by which an event is evaluated are organized into what's called trigger paths. Trigger paths serve to sort the dataset by the sets of criteria they pass. For paths with a high rate, such as leptons with a relatively low p_T threshold, a trigger path may be prescaled. Prescaling involves only accepting the trigger every n^{th} time, where n is some integer greater than one.

Data collected by the detector system is read and stored into 40 MHz buffers to wait for a trigger decision. If the L1 trigger accepts an event, it is sent for further analysis over a 100 kHz bandwidth network. To enforce the bandwidth, it is sometimes necessary to throttle the trigger. The reduction in event readout, referred to as dead time, is generally kept under 1% of events. Events that are accepted by the L1 trigger go through additional filtering by the

HLT before being stored to tape. The HLT [24] is a software system running on a processing farm with access to event information from all detector systems. The HLT reaches a decision within a time window of less that 200 μs. As with the L1 trigger, evaluation is divided into trigger paths. Computationally expensive operations like track building are performed at the final stages, after many events have been rejected.

CHAPTER 4 SIGNAL AND BACKGROUND PROCESSES

4.1 Signal Process

The W and Z particles are measured indirectly through their decay products. Because their lifetimes are on the order of $\sim 10^{-25}$ s, they do not live long enough to reach the detector. Tables 4.1 and 4.2 show the world average branching fractions of the W and Z bosons.

The majority of WW and WZ events involve fully hadronic decays, meaning that both gauge bosons decay into hadrons. This decay channel is not useful for us, because there is no reliable way to distinguish it from other processes that produce only jets, such as QCD.

There are two fully leptonic channels, $lll\nu$ and $l\nu l\nu$, which involve both bosons decaying leptonically. Past CMS studies have focused on such leptonic channels [27, 28]. These channels, however, suffer from low statistics, due to the fact that the majority of W and Z decays are hadronic.

There are then two semileptonic channels, $lljj$ and $l\nu jj$, where one boson decays hadronically and the other leptonically. The semileptonic channels offer a compromise, giving more statistics than fully leptonic channels, at the expense of dealing with jets in the final state.

This analysis was based on measurements of the $l\nu jj$ channel, with the charged lepton being either an electron or a muon. Events with both positively and negatively charged leptons were used. The $l\nu jj$ channel has the advantage of higher statistics than the $lljj$

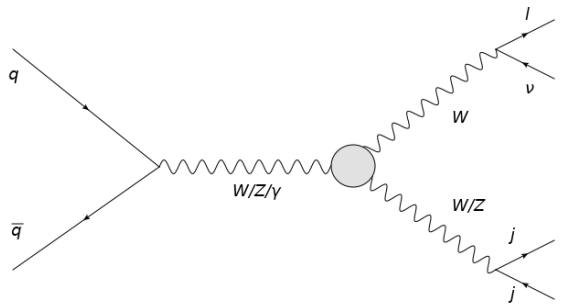

Figure 4.1: The channel that was used for this analysis is the $l\nu jj$ channel, with a W decaying leptonically into a charged lepton and a neutrino, and a W or Z decaying hadronically. The charged lepton was either an electron or a muon.

Table 4.1: Decay modes of the W boson.

W decay mode	fraction
hadrons	67%
$e\ \nu$	11%
$\mu\ \nu$	11%
$\tau\ \nu$	11%

Table 4.2: Decay modes of the Z boson.

Z decay mode	fraction
hadrons	70%
$\nu\ \overline{\nu}$	20%
$e\ \overline{e}$	3.3%
$\mu\ \overline{\mu}$	3.3%
$\tau\ \overline{\tau}$	3.3%

channel, at the expense of dealing with a neutrino. Figure 4.1 shows the tree level Feynman diagram for the decay channel used in the analysis. There have been past studies in semileptonic channels [29] at energies of 7 and 8 TeV. The study that this thesis builds off of [30] was the first to look at the semileptonic channel at 13 TeV.

4.2 Background Processes

There were four processes that contributed to background in this analysis. The primary background process was W+jets, where a W boson is produced along with one or more jets, and the W decays leptonically, mimicking the signal signature, as shown in Figure 4.2. The secondary background was $t\bar{t}$, involving a top-antitop quark pair decaying into W bosons and b-quarks, as shown in Figure 4.3. Finally, there was a minor background from single top, which involves a W decaying into a top-bottom quark pair, and the top decaying into a W and b-quark, as shown in Figure 4.4. In addition to these background processes, general QCD events that involve jets faking gauge boson decays and leptons were taken into account. These processes were not simulated with Monte Carlo, but were modeled by data, as described in Chapter 7.

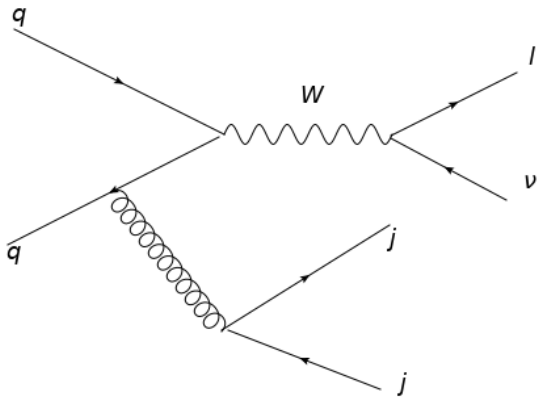

Figure 4.2: Example W+jets background process.

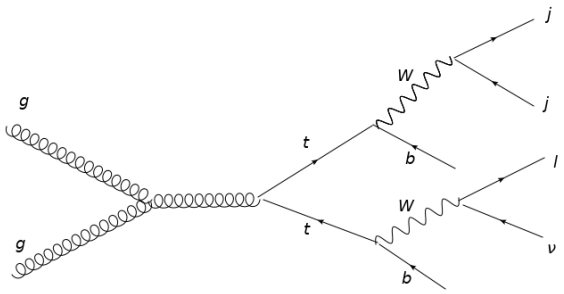

Figure 4.3: Example $t\bar{t}$ background process.

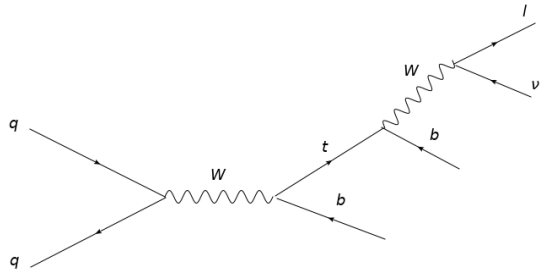

Figure 4.4: Example single top background process.

CHAPTER 5 PARTICLE IDENTIFICATION, SELECTION, AND RECONSTRUCTION

General Event Selection

Various selection requirements were placed on events to eliminate background processes. Events were required to have at least one well-reconstructed collision vertex. The reconstructed collision vertex with the highest summed p_T^2 was designated as the primary vertex [31].

The particle flow algorithm [32] was used to reconstruct and identify each particle in an event using information from the different elements of the CMS detector.

5.1 Electron Selection

For electron events there must be an electron within the pseudorapidity range of $|\eta| < 2.5$, with a minimum p_T of 50 GeV. The p_T trigger threshold for electron candidates was 45 GeV, and they had to be within the pseudorapidity range of $|\eta| < 2.5$, but outside of the $1.44 < |\eta| < 1.57$ range. The latter requirement was to avoid poor reconstruction due to a gap between the barrel and endcap of the ECAL system. An additional trigger requirement existed if its p_T was less than 115 GeV; an isolation cone of $\Delta R < 0.3$ was placed around electrons whose p_T were less than 115 GeV, where

$$\Delta R = \sqrt{(\Delta\eta)^2 + (\Delta\phi)^2}, \tag{5.1}$$

is the distance in the rapidity-azimuthal plane between two objects. The scalar sum p_T from all the particles in the cone must be less than 5 GeV; $\sum_i |p_{Ti}| < 5$ GeV. In addition to these requirements, there had to be no more than one lepton, to avoid fully leptonic $t\bar{t}$ events. For the purposes of rejection, there were looser requirements on leptons. In order to be used to reject an event, an electron had to have a p_T of greater than 35 GeV. Electrons were reconstructed through a combination of information from the central tracking detector and the ECAL [33, 34].

5.2 Muon Selection

For muon events there had to be a muon with p_T greater than 53 GeV and within the pseudorapidity range of $|\eta| < 2.4$. Muons were reconstructed by combining tracks in the muon system and inner tracker [35, 36]. The p_T trigger threshold for muon candidates was 50 GeV, and they had to be within the pseudorapidity range of $|\eta| < 2.4$. The isolation requirement for muons was that the scalar sum of the p_T tracks within $\Delta R < 0.3$ be less than 10% of the muon's p_T. The loose p_T requirements for a muon for the purpose of rejecting an event with more than one lepton, were that it have a p_T greater than 20 GeV.

5.3 Jets and Jet Selection

Because they have color charge, quarks do not exist as free particles, but instead form into hadrons. This process is called hadronization, or fragmentation [6]. The color field around a quark creates multiple quark-antiquark pairs, leading to multiple particles being detected. A cluster of particles that appears in the detector is then identified as a jet. There is no definitive answer to the question of how many jets are present in an event. Jets are defined by jet algorithms, and different algorithms may define different numbers of jets. In this study, the jet pairs coming from the W or Z bosons were boosted, with an energy of at least 200 GeV, and tended to appear as a single 'fat' jet [30]. The jet algorithm used in this analysis was the anti-kT algorithm [37]. The anti-kT algorithm is known as a recombination algorithm. It works by defining a distance between pairs of particles, performing successive recombinations of pairs of closest particles, and stopping when all particles are too far apart. The distance, d_{ij}, is defined as

$$d_{ij} = \min\left(k_{t,i}^{2p}, k_{t,j}^{2p}\right)\left(\Delta y_{ij}^2 + \Delta\Phi_{ij}^2\right)/R^2, \tag{5.2}$$

where Δy and $\Delta\Phi$ are the rapidity and azimuthal angle differences between two particles, and k_t is the transverse momentum. Rapidity is defined by the relation

$$y = \frac{1}{2} \ln \left(\frac{E + p_z}{E - p_z} \right), \tag{5.3}$$

where E is a particle's energy and p_z is the component of the particle's momentum along the beam direction. The exponent p has different values for different jet algorithms, but it has a value of -1 for the anti-kT algorithm. The constant R is a dimensionless parameter that can be varied within a single algorithm. There were two types of jets that were reconstructed for this analysis, both constructed using the anti-kT algorithm. Jets formed with a distance parameter of R=0.4 and R=0.8 are referred to as AK4 and AK8 jets, respectively. The AK8 jets were the jets that were used to identify signal events, while the AK4 jets were used to reject events involving top quark decays. Each event was required to have an AK8 jet with a minimum p_T of 200 GeV, and within the pseudorapidity range of $|\eta| < 2.4$. In order to reduce top background, events with AK4 jets of p_T greater than 30 GeV and within the same pseudorapidity range were rejected. The AK8 jet with the highest p_T was used for the hadronically decaying gauge boson.

5.3.1 PUPPI

Pileup (PU) occurs when particles from other proton-proton collisions appear to come from the collision of interest. Because they don't come from the collision of interest, identifying and removing these particles is important. The method for removing PU in this analysis was PileUp Per Particle Identification (PUPPI) [38]. Tracking is available for charged particles, and this allows for determination of whether a given particle is from the collision of interest or not. Using this knowledge from charged particles, information can be gained about the p_T spectrum of PU versus non-PU particles. This knowledge is used to assign a value to neutral particles ranging from 0 to 1, indicating the likelihood that it comes from the collision of interest.

5.3.2 Soft Drop Mass

A useful quantity in the analysis was the softdrop mass of the jet [39]. Soft Drop is a procedure to remove soft and wide-angle radiation from a jet in order to mitigate effects of pileup, initial state radiation (ISR), and underlying event (UE). Radiation emitted by incoming particles before they collide is ISR. Particles that come from the remnants of the protons involved in the collision of interest are UE particles. The softdrop procedure involves breaking a jet of radius R_0 into two subjets. If the condition

$$\frac{\min(p_{T1}, p_{T2})}{p_{T1} + p_{T2}} > z_{cut} \left(\frac{\Delta R_{12}}{R_0} \right)^{\beta} \tag{5.4}$$

is met then the jet is kept as is. In Equation 5.4, ΔR_{12} is defined as the distance in the rapidity-azimuthal plane, as defined in Equation 5.1, between subjets 1 and 2, Otherwise, the smaller p_T subjet is dropped and the procedure is applied again, with two new subjets. The variables z_{cut} and β are adjustable depending on how much grooming is needed. In the analysis, z_{cut} was set to 0.1 and β was set to 0.

5.3.3 N-Subjettiness

Another useful quantity for jet selection in this analysis was N-subjettiness [40]. For a jet with N subjet candidates, N-subjettiness is defined as,

$$\tau_N = \frac{1}{d_0} \sum_k p_{T,k} \min\{\Delta R_{1,k}, \Delta R_{2,k}, ..., \Delta R_{N,k}\}, \tag{5.5}$$

where $p_{T,k}$ is the p_T of the k^{th} constituent particle, $\Delta R_{j,k}$ is the distance between the k^{th} constituent particle and the j^{th} subjet candidate, as defined in Equation 5.1. The overall normalization factor in Equation 5.5, denoted as d_0, is defined as

$$d_0 = R_0 \sum_k p_{T,k}, \tag{5.6}$$

where R_0 is the jet radius. The ratio $\tau_{21} = \tau_2/\tau_1$ was used to place selections on jets in this analysis.

5.4 Missing Transverse Momentum Selection

Neutrinos are not measured directly. Instead, their existence must be inferred from momentum imbalances. In this study, their kinematic values were inferred using the missing transverse energy (MET) in the collisions, the kinematics of the lepton, and constraining the lepton and neutrino to the W boson mass. Transverse energy is defined in terms of mass and transverse momentum as,

$$E_T^2 = p_T^2 + m^2. \tag{5.7}$$

In the case of neutrinos, mass is (effectively) zero, and so E_T and p_T are equivalent. The minimum MET for an event was 110 GeV for an electron event and 40 GeV for a muon event, in order to reject multi-jet QCD events. The higher threshold for the electron channel was placed in order to avoid QCD jets mismeasured as electrons.

5.4.1 Calculating Longitudinal Neutrino Momentum

The components of momentum perpendicular to the beam axis (transverse momentum) are zero in the initial state of colliding protons, and therefore must be zero after the collision. The longitudinal momentum of the collision cannot be balanced out in this way, because particles whose momentum is nearly all longitudinal will travel down the beam pipe and not be detected. The transverse momentum imbalance of measured final state particles was used to estimate the neutrino's transverse momentum.

The energy-momentum relation for the leptonic W is

$$W_m^2 = (l_E + \nu_E)^2 - (\vec{l}_{pT} + \vec{\nu}_{pT})^2 - (l_z + \nu_z)^2. \tag{5.8}$$

Here, l_E and ν_E are the lepton and neutrino energies, l_z and ν_z are the lepton and neutrino z momenta, and l_{pT} and ν_{pT} are the transverse momentum for the lepton and neutrino. The leptonic W was assumed to have its pole mass of 80.4 GeV for the purpose of the calculation.

The energy-momentum relation equation for the neutrino, neglecting neutrino mass, is

$$\nu_E^2 = \nu_{pT}^2 + \nu_z^2. \tag{5.9}$$

(The neutrino mass is not currently known, but upper limits on it are on the order of eV for the electron neutrino, and MeV for the tau and muon neutrinos, all of which are negligible for the energies involved with this study [41, 42].) The variable a is defined for convenience as

$$a = W_m^2 - l_m^2 + 2(\vec{l}_{pT} \cdot \vec{\nu}_{pT}), \tag{5.10}$$

where l_m is the mass of the lepton. Using Equation 5.10, Equation 5.8 can be rewritten as

$$l_E \nu_E = \frac{1}{2}a + l_z \nu_z. \tag{5.11}$$

Substituting ν_E from Equation 5.11 into Equation 5.9 gives the quadratic equation for ν_z:

$$(l_E^2 - l_z^2)\nu_z^2 - a l_z \nu_z + l_E^2 \nu_{pT}^2 - \frac{1}{4}a^2 = 0. \tag{5.12}$$

Note that, because Equation 5.12 is a quadratic equation, it will give two solutions for ν_z. The two solutions were both real and distinct around 85% of the time. The other 15% of the time they were both imaginary. In such cases, the real portion was taken as the solution. The third possible outcome for a quadratic, to have two identical real solutions, occurred well under 1% of the time.

5.4.2 Choosing the Correct Neutrino Solution

In the majority of cases, there were two distinct real solutions for the neutrino's longitudinal momentum. A method was needed for selecting which of them to use for calculations. To more rapidly generate events to test neutrino p_z selection schemes, a toy Monte Carlo program was written. It simulated a WW system, with one W decaying into quarks, and the other into a charged lepton and a neutrino. For speed, the toy Monte Carlo used a ran-

dom number generator to produce the smearing of measured quantities that would normally come from detector effects. The selections that were placed on the events were applied to the toy simulation. Once the toy gave results, they were verified by being placed into full simulation. The task was to select the solution that is closer to the true value. Several methods were investigated to select the best solution, and the results were compared to the truth information. The difference between the generator level information and the selection scheme is shown in Figure 5.1, while the difference between the generated p_z value and the value rejected by the selection scheme is shown in Figure 5.2.

- **Method 0:** Select the solution that is closer to the generator level truth information; a way of cheating, just to get a feel for the best possible performance from any selection scheme.
- **Method 1:** Select the solution that is further from the z momentum of the lepton.
- **Method 2:** Same as above, but if either solution is above 300 GeV in absolute value, select the lower one in absolute value.
- **Method 3:** Select the solution that is smaller in absolute value. It does better than methods one or two.
- **Method 4:** Select the solution that causes the lepton-neutrino pair to be closer to the z axis in its direction.
- **Method 5:** Select the solution that causes the leptonic W to have a smaller z momentum.
- **Method 6:** Select the solution that minimizes the z momentum of the entire WW system.
- **Method 7:** Select the solution that minimizes the mass of the overall WW system.

The histograms were produced by subtracting the generator level neutrino p_z from the reconstructed value. The histogram in Figure 5.1 uses the reconstructed values that were chosen by the selected method, while the histogram in Figure 5.2 uses the values that were rejected by that method. The better a method performs, the sharper the peak will be at the zero point of the histogram in Figure 5.1. All methods will have some spread, due to the fact that both solutions to the quadratic equation are affected by measurement error, and so even method 0 does not perform perfectly. The difference in shape between Figures 5.1 and 5.2 is a measure of the efficiency of the selection method. If a method were completely random, with a fifty/fifty chance of selecting the better solution, one would expect to see a similar shape in Figures 5.1 and 5.2. The most striking difference is for method 0, where there's a gap instead of a peak at the center for the rejection histogram. Among the methods investigated, method 3 has the highest peak in Figure 5.1, and the lowest dip in Figure 5.2, and so it was chosen. Note that method 5 is not shown in Figures 5.1 or 5.2. This is because it always gave identical results to method 3. Note that method 5 involves adding the z momenta of the lepton and neutrino, and minimizing the absolute value of the sum, while method 3 only involves minimizing the absolute value of the neutrino z momentum. If the lepton and neutrino z momenta are always pointing in the same direction, then these methods will necessarily give the same result.

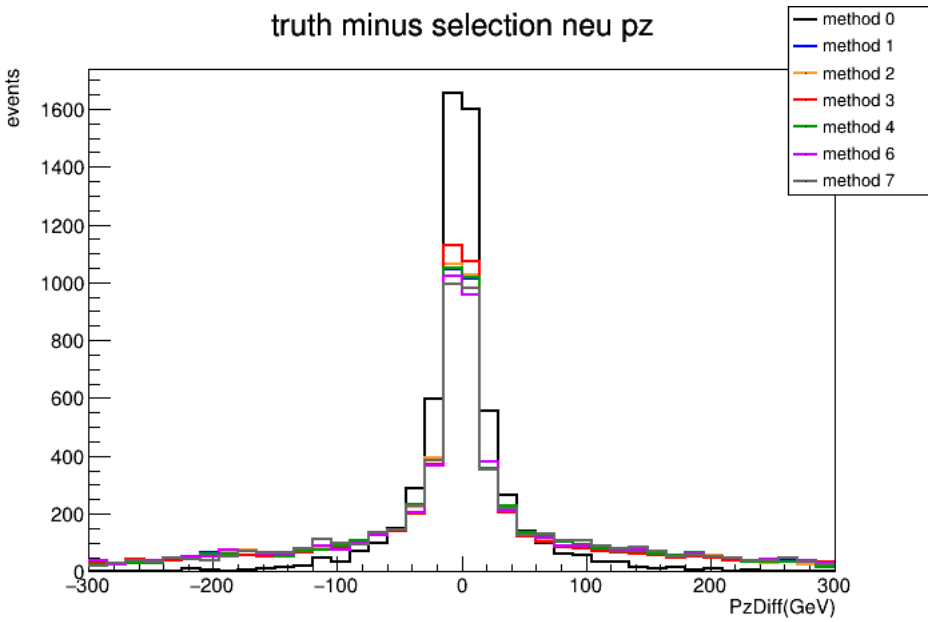

Figure 5.1: The difference between truth information for the neutrino p_z and the reconstructed solution chosen by the given selection method.

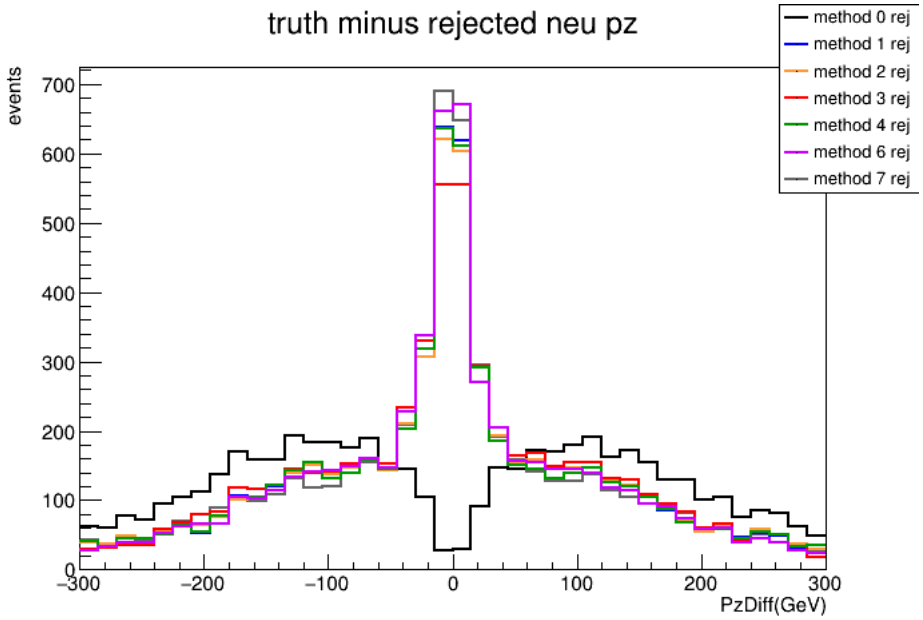

Figure 5.2: The difference between truth information for the neutrino p_z and the reconstructed solution rejected by the given selection method.

CHAPTER 6 MONTE CARLO

6.1 Signal Simulation

The MadGraph [43] program was used to generate the Monte Carlo simulation of the signal processes at next to leading order (NLO). MadGraph is a matrix element generator. It calculates cross sections for tree level processes. It also allows for beyond the standard model (BSM) models to be imported for simulation, and allows the user to adjust parameters specific to the BSM model, as well as basic parameters like particle masses.

The hard scattering process involves the initial interaction of the partons in the colliding protons. The internal structure of the proton is expressed in terms of parton distribution functions (PDFs), which express the probability for quarks and gluons in the proton to have a fraction, x, of the proton's total momentum. To estimate the cross section of a given event, $pp \to X$, it is necessary to sum over the quark, anti-quark, and (depending on the process) gluon configurations, and for each of these, integrate the PDFs. The differential cross section,

$$\frac{d\sigma\left(pp \to X\right)}{d\Omega} = \sum_{q\overline{q}} \int dxdy f_q\left(x, Q^2\right) f_{\overline{q}}\left(y, Q^2\right) d\sigma\left(q\overline{q} \to X\right), \tag{6.1}$$

is defined as an infinitesimal element of solid angle, $d\Omega = \sin\theta d\theta d\phi$. The integration variables x and y are the quark and antiquark fractions of the proton's overall momentum. The functions, $f\left(x, Q^2\right)$ are the parton density functions for a proton at energy Q. In this case, the processes were $pp \to W^{\pm} \to W^{\pm}Z$ and $pp \to Z/\gamma^* \to W^+W^-$, followed by the decays $W/Z \to jj$ and $W \to l\nu$.

6.1.1 Multi-Weighting

One feature of MadGraph is that it allows for multiple weights to be assigned to a process, corresponding to different values of a parameter. This saves considerable computing time and resources. The original intention of this project was to study the five aTGC parameters obeying $SU(2) \otimes U(1)$ symmetry. Due to an unfortunate software bug, the two CP-odd couplings could not be included. Therefore, only three aTGC parameters were able

to be studied, and simulations with different values of them were needed. The reweighting was performed with different values for the electroweak parameters described in Section 2.4.

The weighting for this study was done at leading order, and the new weight of a given event is

$$W_{\text{new}} = \frac{|M_h^{\text{new}}|^2}{|M_h^{\text{old}}|^2} W_{\text{old}}. \tag{6.2}$$

Here, $|M_h|^2$ is the matrix element of the event and W is the weighting of the event. The superscript *old* refers to the default weighting and matrix element, while the superscript *new* refers to the weighting and matrix element selected for a given set of parameters. The initial simulation was done with each parameter set to the maximum (positive) value to be considered for that parameter. Then, each event was reweighted according to each of the other scenarios under consideration (including the standard model, with all aTGC values set to 0), with aTGC values. This process saves much computational time and storage space when compared to running a separate simulation for each combination of values of the parameters. A limitation of this method is that there is a danger that there will be areas of phase space where an event occurs with a non-negligible probability in one scenario, but not another. Therefore, the scenario that was used as the default for the simulation, before reweighting, was the one expected to have the most events in most areas of phase space. This is why each parameter was set to its maximum value to be considered. In this case, if a certain region of phase space has a rather small amplitude in the standard model for instance, but a high amplitude with all of the aTGC values set to their maximum, an event that occurs in this region will simply have a very low weighting associated with the standard model. However, if the standard model were to be used as the default scenario, then there may be no events in this region to weight, or only one, which would then gain a ridiculously high weighting associated with the aTGC values. To confirm that the multi-weight method gave an accurate answer, small initial samples were run with the standard model only, and this was compared to standard model events from the multi-weighted sample. Afterwards, weights need to be checked to make sure all are on the order of unity or smaller; an excessively

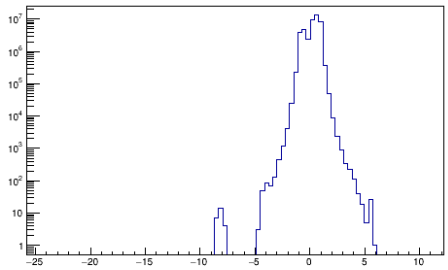

(a) WW Events in the Muon Channel.

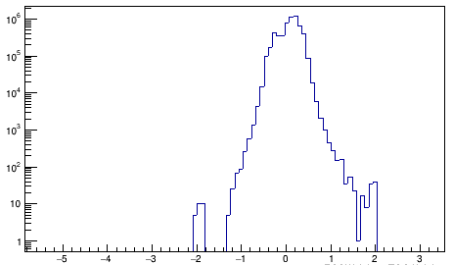

(b) WZ Events in the Muon Channel.

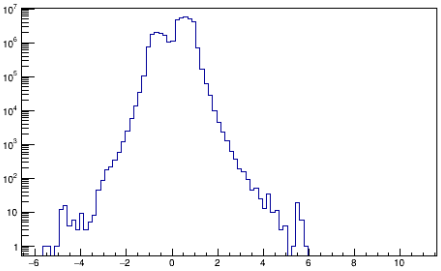

(c) WW Events in the Electron Channel.

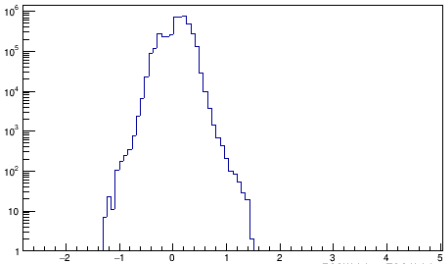

(d) WZ Events in the Electron Channel.

Figure 6.1: A distribution of the weights for events generated for the signal Monte Carlo for WW and WZ events in the electron and muon channels. Nearly all weights are of the order 1 or less.

large weight could indicate that a given area of phase space needs more events simulated. Figure 6.1 shows the weight distributions for the WW and WZ events, in the electron and muon channels. Note that there are some negative weights. Negative weights occur due to statistical errors [44], but are few enough that they do not allow for an overall negative number of events to occur in a reasonably sized bin. The three CP-even couplings were each given five possible values, including the standard model, leading to a total of 125 different parameter combinations. Table 6.1 shows the values generated for the various parameters. These values were chosen based on limits set by previous analyses.

6.2 Standard Model Signal Simulation

Because the signal processes were generated with nonzero values for anomalous couplings, and then the standard model was regained after the fact, a purely standard model Monte Carlo of both WW and WZ events was also generated, as a means of providing a cross check,

Table 6.1: Values used for the anomalous trilinear gauge couplings.

parameter	values (TeV^{-2})				
c_{WWW}/Λ^2	-3.6	-1.8	0.0	+1.8	+3.6
c_W/Λ^2	-4.5	-2.25	0.0	+2.25	+4.5
c_B/Λ^2	-20.0	-10.0	0.0	+10.0	+20.0

due to the issues raised in Section 6.1.1.

The standard model WZ Monte Carlo, like the anomalous coupling Monte Carlo, was generated with MadGraph, while the standard model WW Monte Carlo was generated with Powheg [45], both at NLO. The cross sections for the standard model WW and WZ signal were scaled to match the predictions of Refs. [46] and [47], respectively, both at next-to-next-to-leading order (NNLO).

6.3 Background Process Simulation

Madgraph was also used to simulate the W+jets background, and the s-channel of the single top background, both at NLO. Powheg was used to simulate $t\bar{t}$ background, and the t- and tW-channels of the single top background, also at NLO.

6.3.1 Background Process Cross Section Calculation

To normalize the background processes, an overall cross section was calculated, with uncertainties. Fitting MC derived distributions to data was used to refine the normalization within the uncertainties, as discussed in Section 7.3. The cross sections for the $t\bar{t}$ background was calculated using Top++ [48], at NNLO for QCD, and next-to-next-to-leading log (NNLL) for soft gluon radiation. For the single top processes, MCFM [49] was used to calculate the overall cross section at NLO. The W+jets background was derived from data, as discussed in Section 7.2.

6.4 Hadronization and Showering

After the initial hard scattering was generated, further processing was passed on to Pythia [50] for hadronization. Pythia was responsible for showering, and for hadronizing the quarks once they are produced.

6.4.1 Parton Showers

The incoming partons within the protons will radiate photons and gluons before the hard process takes place. This is known as initial state radiation (ISR). Similarly, the outgoing particles will radiate photons and gluons, known as final state radiation (FSR). It would be prohibitively difficult to make exact calculations for such processes, as they involve a large number of higher order loops. Another approach is therefore taken with PYTHIA, the parton-shower approach. An arbitrary number of branchings of one parton into more is combined to yield a description of multi-jet events. Approximations of full expressions are derived from simplifying the kinematics. Processes such as $q \to qg$ and $e \to e\gamma$ are substantially similar regardless of the underlying event, and this allows them to be calculated independently.

6.4.2 Hadronization

Hadronization (also called fragmentation) involves the creation of quark-antiquark pairs in the vacuum, and the binding of them to form colorless hadrons. This occurs when the parton shower reaches an energy at which perturbative QCD becomes invalid [50], around 1 GeV. This process is not understood from first principles, but rather is approximated using phenomenological models. The Lund string model [50] is used by PYTHIA for hadronization. In this model, as two quarks move apart, a gluon string forms between them. As the distance increases between the quarks, the potential energy linearly increases, and it eventually becomes energetically favorable for a new quark-antiquark pair to be formed, breaking the gluon string. The subsequent decay of unstable hadrons is also sometimes referred to as part of hadronization, and is handled by PYTHIA as well.

6.5 Detector Simulation

The detector response in the Monte Carlo was simulated using the GEANT4 package [51]. After hadronization and showering are completed, particles enter the detector, and the response must be simulated as well. The GEANT4 software takes into account the geometry of the detector, the materials that the detector is composed of, and the detector's magnetic field. Using this information, the software is able to simulate how particles interact with

matter, both electromagnetically and via the strong interaction. This information is then used to simulate the electronic responses of the subdetectors. The output of GEANT4 is in the same format as the detector's output, allowing the same algorithms to be used in reconstructing data and Monte Carlo.

CHAPTER 7 PROCESS MODELING

Diboson mass is defined as

$$M_{WV}^2 = (E_{\text{jets}} + E_{\text{lep}} + E_\nu)^2 - (p_{\text{jets}} + p_{\text{lep}} + p_\nu)^2. \tag{7.1}$$

In Equation 7.1, p_{jets} and E_{jets} are the combined momentum and combined energy of the jets, respectively; p_{lep} and E_{lep} are the momentum and energy of the charged lepton; and p_ν and E_ν are the momentum and energy of the neutrino.

7.1 Signal Modeling

For signal events simulated with and without anomalous couplings, the diboson mass distribution followed an exponentially falling distribution to a good approximation to data. For the simulated signal process, the diboson mass distribution was modeled as [30]:

$$F(M_{WV}) = N_{00}e^{a_{\text{corr}}M_{WV}} + \sum_{i\leq j} N_{ij}c_i c_j e^{a_{ij}M_{WV}} \left[\hat{\delta}_{ij} + \delta_{i0}\delta_{j0} + \delta_{ij}\hat{\delta}_{i0}\left(\frac{1+\text{Erf}((M_{WV}-b_i)/d_i)}{2}\right)\right]. \tag{7.2}$$

The symbol $\hat{\delta}_{ij}$ in Equation 7.2 is defined to be $1-\delta_{ij}$, to represent inequality between the two indices. The c_i terms are the anomalous parameter values to be measured; for $i > 0$, $c_i = \frac{c_W}{\Lambda^2}, \frac{c_B}{\Lambda^2}, \frac{c_{WWW}}{\Lambda^2}$, and $c_0 = 1\,\text{TeV}^{-2}$ is a dummy coefficient used for the standard model portion, for inclusion into the summation. For each of the 125 combinations of values of anomalous parameters given in Table 6.1, the values of each c_i were plugged in, and the other parameters were determined from the multiweighted MadGraph simulation.

Terms in the sum with $i \neq j$ and $i, j \neq 0$ are interference terms between anomalous parameters. Terms with $i = j \neq 0$ are pure anomalous coupling terms, while terms with $i = 0 \neq j$ are interference terms between the standard model and anomalous couplings. Finally, the term with $i = j = 0$ is the pure standard model term. The term with a_{corr} is a correction factor that accounts for the deviation of the standard model from a pure exponential function at higher values of M_{WV}. The N_{ij} are normalization constants, while a_{ij}, b_i, and d_i are parameters determining the shape of the fit. The normalization constant,

N_{00}, for the standard model is fixed to the overall NNLO cross section for the standard model signal as discussed in Section 6.2. The other normalization constants were fit relative to N_{00} using the multiweighted MadGraph simulation. Equation 7.2 can be seen modeling signal Monte Carlo in Figures 9.1 to 9.4.

7.2 Background and SM Signal Modeling

For the background and standard model signal processes, the shape of the diboson mass distribution was fit to the following analytical function [30]:

$$F(M_{WV}) = e^{\left(aM + \frac{b}{M}\right)}, \tag{7.3}$$

where a and b were estimated from simulation or data. However, for limits in which a selection was placed on the angle θ^*, Equation 7.3 was replaced by the analytical function:

$$F(M_{WV}) = e^{\left(\frac{M}{aM+b}\right)}, \tag{7.4}$$

for the W+jets background. Equation 7.4 had been used in the previous analysis [30] as an alternate fitting function for the W+jets background in order to calculate the shape uncertainty. After the angular cuts, the alternate fitting function was able to model the MC, but not the original Equation 7.3. The lack of a second fitting function to model the background means that the estimate for the shape uncertainty of the W+jets cannot be computed. Equation 7.3 can be seen fit to the data before any angular selection in Figure 9.9. Equations 7.3 and 7.4 can both be seen fit to data after an angular selection was applied in Figure 9.15.

For the single top background and standard model signal, the shape and normalization were determined from simulation. For the $t\bar{t}$ background, the shape was determined from simulation, whereas the normalization was determined from data in a control region. In order to fit for the values of a and b for the W+jets background, as well as to normalize, different control regions were used. In order to separate the control regions from the signal region,

Table 7.1: These cuts were placed on all events, signal and background.

Signal Requirement
lepton $p_T > 50(e)$ $53(\mu)$ GeV
jet $p_T > 200$ GeV
$\tau_{21} < 55$
W $p_T > 200$ GeV
WW mass > 900 GeV
MET $> 110(e)$ $80(\mu)$ GeV
$\lvert\Delta R(j,l)\rvert > \pi/2$
$\lvert\Delta\Phi(j,l)\rvert > 2$
$\lvert\Delta\Phi(j,MET)\rvert > 2$

softdrop jet mass, as described in Section 5.3.2, was used, as well as b-tagging. Control regions designed to enhance the W+jets background included events with no b-tagged jets, and with a softdrop mass within ranges outside the signal region. The lower W+jets control region included events with a softdrop mass between 40 and 65 GeV, and the upper W+jets control region included events with a softdrop mass between 105 and 150 GeV. The results of the fitting, before and after angular selection, can be seen in Chapter 9.

In addition to this, there was a control region designed to enhance $t\bar{t}$ background, which consisted of events with a softdrop mass between 40 and 150 GeV, and one or more b-tagged jets. The signal region contained events between the two W+jets control regions, with a softdrop mass between 65 and 105 GeV, and no b-tagged jets. The signal region, the W+jets control regions, and the $t\bar{t}$ control region are shown in Figure 7.1. In addition, there were general cuts that were placed on all events that were modeled, as shown in Table 7.1. These were applied to further reduce background and enhance signal. In Figure 7.2 shows the distribution of Monte Carlo events in the signal and W+jets background regions, compared with the data after unblinding.

While Figure 7.2 shows distributions before angular selections were placed, Figures 7.3 and 7.4 show distributions after angular selections of $|\cos\theta_1| < 0.6$ and $|\cos\theta^*| < 0.8$, respectively, giving an indication of the background discriminating power of the angular variables.

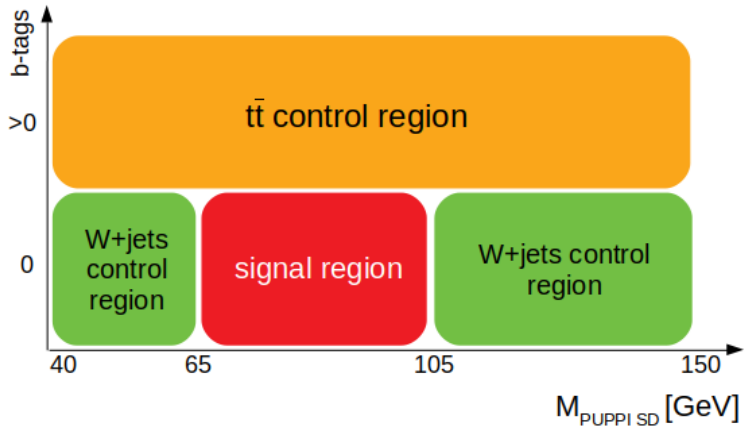

Figure 7.1: The signal and control regions were defined based on the soft drop PUPPI mass and number of b-jets in the event.

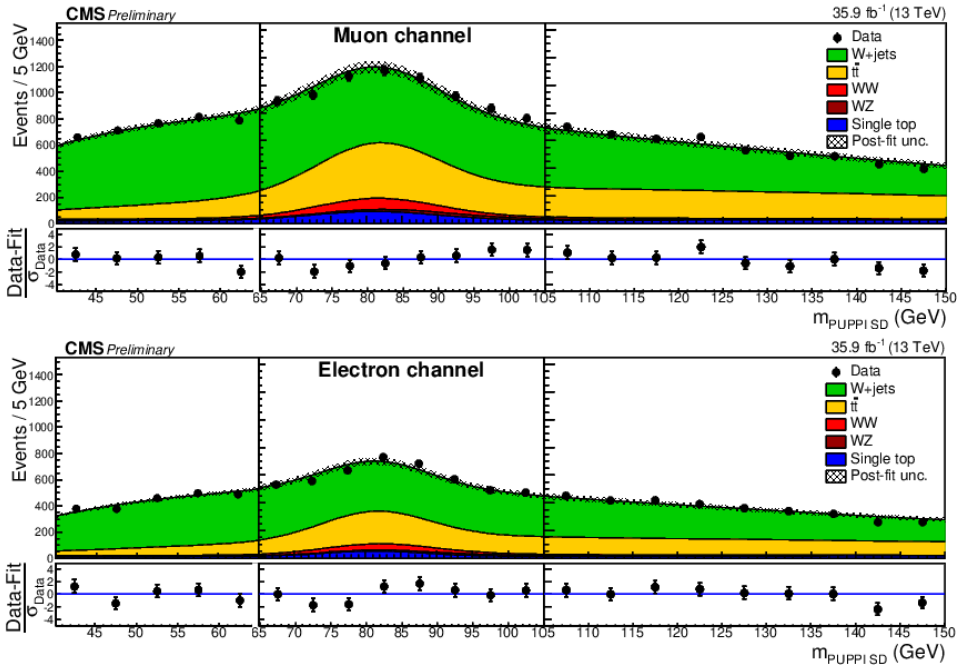

Figure 7.2: Event distributions in the signal and W+jets background regions after unblinding. These distributions are before any angular selections were placed on the data.

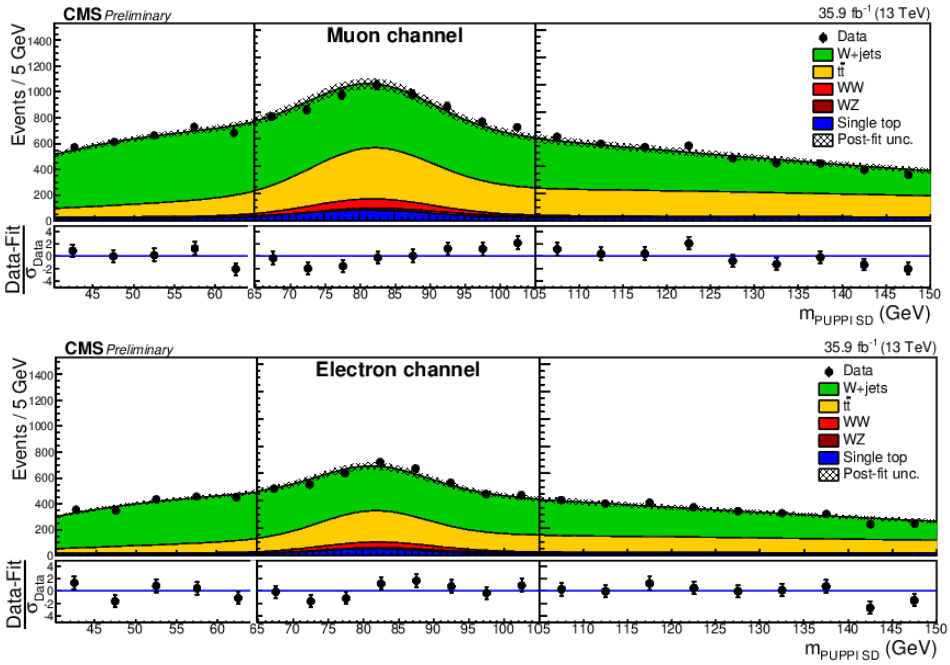

Figure 7.3: Event distributions in the signal and W+jets background regions after unblinding. These distributions are after an angular cut of $|\cos\theta_1| < 0.6$ was placed on the data.

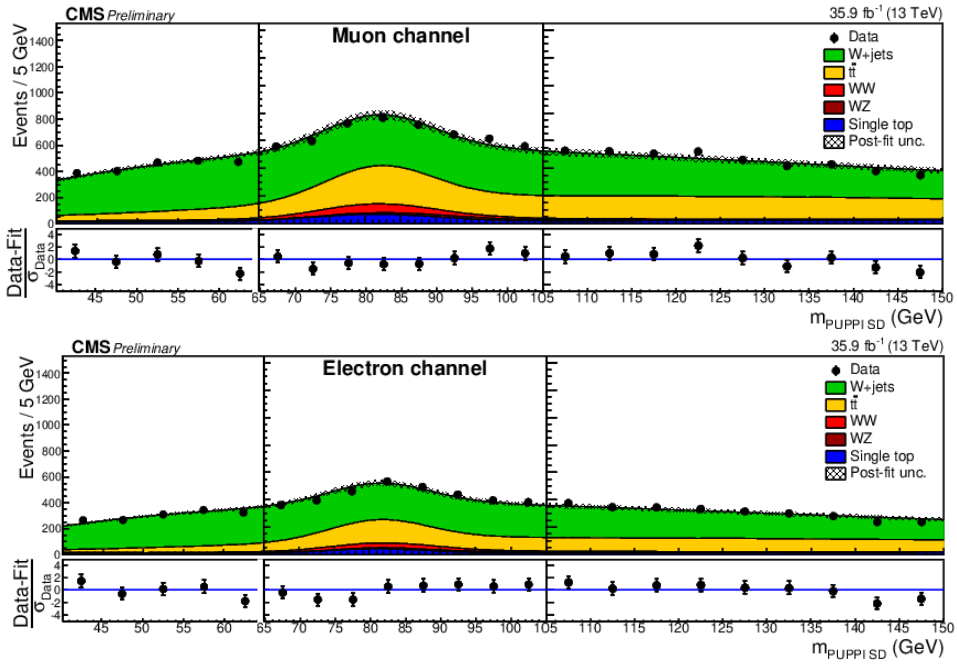

Figure 7.4: Event distributions in the signal and W+jets background regions after unblinding. These distributions are after an angular cut of $|\cos\theta^*| < 0.8$ was placed on the data.

Table 7.2: Signal and various background processes were generated with Monte Carlo and adjusted with data from control regions. Here, MC means fixed by simulation, MC±FIT means fixed by simulation within uncertainties and adjusted using data, and FIT means allowed to vary freely during the data fit.

Process	m_{WV} shape	norm.
W+jets	MC±FIT	FIT
$t\bar{t}$	MC±FIT	MC±FIT
s-top	MC	MC±FIT
signal	MC	MC±FIT

7.3 Alpha Ratio Method

To calculate the M_{WV} shape and normalization of the W+jets background, the alpha ratio method [52] was used. The basic premise behind the alpha ratio method is to assume that the ratio of the true shape function to that given by simulation is the same in both the signal and background region:

$$\frac{F_{\mathrm{DT}}^{\mathrm{SR}}\left(m_{WV}\right)}{F_{\mathrm{MC}}^{\mathrm{SR}}\left(m_{WV}\right)} \simeq \frac{F_{\mathrm{DT}}^{\mathrm{CR}}\left(m_{WV}\right)}{F_{\mathrm{MC}}^{\mathrm{CR}}\left(m_{WV}\right)}, \tag{7.5}$$

where the superscripts SR and CR indicate signal region and control region, and the subscripts DT and MC indicate data and Monte Carlo. In the control region, the background process was dominant and thus contamination in the data from signal or other background processes was minimal. This was checked with the signal simulation. Then, $F_{\mathrm{DT}}^{\mathrm{SR}}\left(m_{WV}\right)$ was calculated from Equation 7.5. The alpha ratio method was used for the $t\bar{t}$ background from its control region, and then it was used for the W+jets background from its two control regions. The alpha function is defined as

$$\alpha\left(m_{WV}\right) = \frac{F_{\mathrm{MC}}^{\mathrm{SR}}\left(m_{WV}\right)}{F_{\mathrm{MC}}^{\mathrm{CR}}\left(m_{WV}\right)}, \tag{7.6}$$

giving the final equation for the function of m_{WV} as

$$F_{\mathrm{MC}}^{\mathrm{SR}}\left(m_{WV}\right) = F_{\mathrm{DT,wjets}}^{\mathrm{CR}}\left(m_{WV}\right)\alpha_{\mathrm{wjets}}\left(m_{WV}\right) + F_{\mathrm{DT},t\bar{t}}^{\mathrm{CR}}\left(m_{WV}\right)\alpha_{t\bar{t}}\left(m_{WV}\right) + F_{\mathrm{MC,stop}}^{\mathrm{SR}}\left(m_{WV}\right) + F_{\mathrm{MC,sgnl}}^{\mathrm{SR}}\left(m_{WV}\right). \tag{7.7}$$

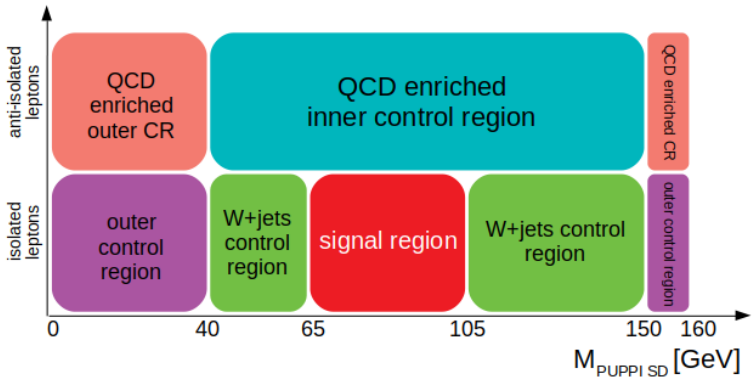

Figure 7.5: The QCD background was estimated from data using control regions defined by an inverted lepton isolation selection.

What was done, therefore, was to use a combination of data and Monte Carlo to extrapolate both shape and normalization of the background processes, using alpha transfer functions to model the background in the signal region. Table 7.2 shows the various processes and how their shapes and normalizations were computed.

7.4 QCD Estimation

Because QCD Monte Carlo is not always reliable, a data driven estimation of the QCD background shape was performed with the help of a QCD enriched control region. In addition to the already present W+jets and $t\bar{t}$ control regions, three new control regions were formed from the data. An outer control region was defined by extending the softdrop mass beyond the edges of the W+jets control regions, as shown in Figure 7.5. Then, the lepton isolation criteria were inverted to form anti-isolated regions. Leptons produced via QCD effects are likely to be surrounded by other particles. Isolation was applied to eliminate QCD. Therefore, anti-isolation was designed to enhance it. The anti-isolated regions consisted of the QCD enriched outer control regions, corresponding to the new outer control regions in softdrop mass, and the QCD enriched inner control region, which corresponded to the signal and W+jets regions in range of softdrop mass. The QCD fake rate was obtained by first taking the ratio of events in the isolated outer control region to those in the QCD-enriched, anti-isolated outer control region. Then, this ratio was multiplied by the number of events in

Table 7.3: QCD estimation from the different regions in the data. The number of events in each region is shown. The ratio is the number of events in the first column divided by that of the second column. This was then multiplied by the fourth column to give the estimation of the number of QCD events in the signal and W+jets control regions.

channel	outer	QCD outer	ratio	QCD inner	inner
electron	507	1700563	0.030%	565450	169
muon	352	2121627	0.017%	1000762	166

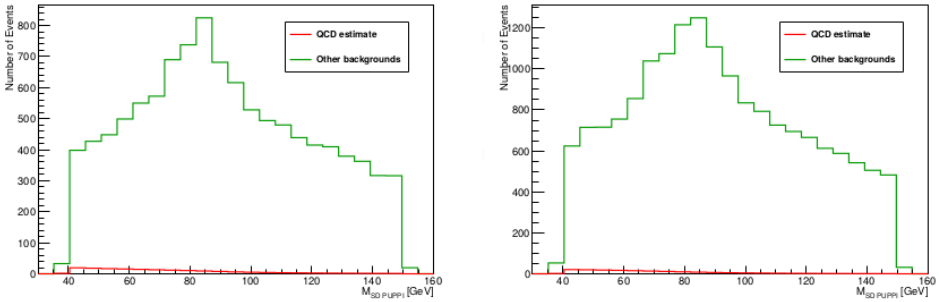

Figure 7.6: Shown [30] is the estimated number of QCD events in the signal region. The green curve represents everything except QCD, including background and standard model signal, while the red curve is projected QCD.

the QCD enriched inner control region to give the estimated number of QCD events in the signal region. As can be seen from the rightmost column of Table 7.3, QCD was not a large background in the signal region. Figure 7.6 also illustrates the lack of a significant QCD background in the signal region.

7.5 Production and Decay Angles

According to Ref. [53], the anomalous couplings κ_γ and λ are related to the magnetic dipole moment μ_W and electric quadrupole moment Q_W of the W boson, while the anomalous couplings $\widetilde{\kappa}_\gamma$ and $\widetilde{\lambda}$ are related to the electric dipole moment d_W and the magnetic quadrupole moment $\widetilde{Q}_W$ of the W boson:

$$\mu_W = \frac{e}{2M_W}\left(1 + \kappa_\gamma + \lambda\right), \tag{7.8a}$$

$$Q_W = -\frac{e}{2M_W}\left(\kappa_\gamma - \lambda\right), \tag{7.8b}$$

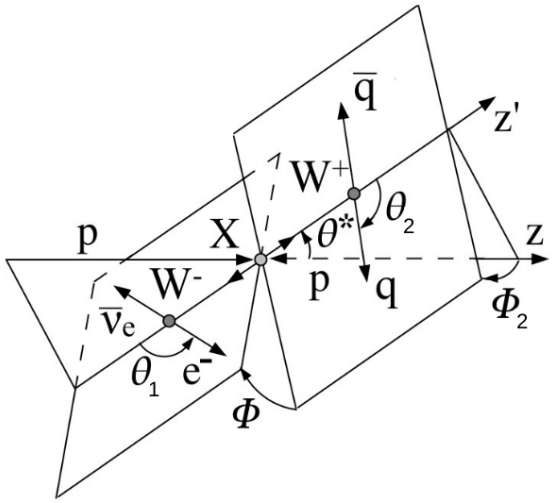

Figure 7.7: A proton-proton to WW event, showing the definitions of angles used to characterize the event.

$$d_W = \frac{e}{2M_W}\left(\widetilde{\kappa}_\gamma + \widetilde{\lambda}\right), \tag{7.8c}$$

$$\widetilde{Q}_W = -\frac{e}{2M_W}\left(\widetilde{\kappa}_\gamma - \widetilde{\lambda}\right). \tag{7.8d}$$

Because these couplings affect the electric and magnetic moments of the W, they affect its helicity, which in turn affects the angles at which its decay products will emerge [53].

The $l\nu jj$ channel has four outgoing particles: two quarks, a charged lepton, and a neutrino. The quarks were reconstructed as jets in the detector, and the neutrino was identified by transverse momentum imbalance in the event.

Five angles were needed to fully describe the decay geometry, shown in Figure 7.7. Because this was a semileptonic channel, there was a leptonically decaying gauge boson, and a hadronically decaying gauge boson, referred to as the leptonic W and the hadronic W or Z. The angle between the incoming protons and the outgoing gauge bosons is labelled θ^*. The cosine of θ^* is what was actually used in the analysis, which varies from -1 to +1. The two incoming protons along with the two outgoing gauge bosons form a plane in the center-of-momentum frame, labelled X in Figure 7.7. (It is assumed that the lab frame is the center-of-momentum frame.) A decay plane can be defined for each gauge boson, contain-

ing the momentum vectors of the boson and its decay products in the center-of-momentum frame. The angle between the hadronic (leptonic) decay plane and plane X in the center-of-momentum frame is Φ_2 (Φ_1). The angle Φ_1 ranges form $-\pi$ to $+\pi$, while the angle Φ_2 ranges from 0 to π because the quark and antiquark were not distinguished from one another in the measurement. The angle between the hadronic and leptonic decay planes is Φ, which also ranges from 0 to π for the same reason as for Φ_2. Among the three angles, Φ, Φ_1, and Φ_2, only two are linearly independent. Of the five angles, three showed potential usefulness for this analysis: θ^*, θ_1, and θ_2. To date, this is the first analysis to use angular variables to place limits on anomalous couplings.

CHAPTER 8 SOURCES OF UNCERTAINTY

Systematic uncertainties were computed for the Monte Carlo simulations of signal and background processes.

Luminosity

There was an overall 2.5% uncertainty in integrated luminosity [54] that affects the overall normalizations of the $t\bar{t}$, single top, and signal Monte Carlo.

Pile-Up

Uncertainty in pileup reweighting of MC events was derived from the uncertainty in the total inelastic cross section used to derive the PU weights [55].

PDFs

Uncertainty in the cross sections used to calculate signal normalization was determined using the uncertainties in the Parton Density Functions, as recommended by Ref. [56].

Factorization and Renormalization

The choice of factorization and renormalization scales introduced some uncertainty, determined by reweighting using all combinations, and taking the largest deviation as the uncertainty [30].

τ_{21} Selection

A 14% normalization uncertainty from mismodeling of the τ_{21} selection efficiency [57] was applied to all calculations derived from hadronic W/Z decays.

b-Tagging and b-Mistagging

Uncertainties in the b-tagging efficiencies [58] existed both for failing to identify b-jets as well as incorrectly identifying them. Inefficiencies from failing to identify b-quark jets had a larger effect on $t\bar{t}$ and single top normalization, while inefficiencies from incorrectly identifying non-b-quark jets had little effect.

JEC and JER

To propagate the uncertainty of the jet energy scale correction (JEC), the energy scale was varied within ± 1 standard deviation. The energy uncertainties for AK4 and AK8 jets

were taken from Ref. [59]. The jet smearing procedure, or jet energy resolution (JER) was repeated after varying the scale factor withing uncertainty.

LEP and LER

Uncertainties in lepton energy scale (LEP) and lepton energy resolution (LER) were also taken into account. Uncertainties in the electron energy scale were taken from Ref. [60], and for muon energy uncertainty, from Ref. [61]. The resolution uncertainty of electrons and muons were taken from the same references, respectively.

Lepton Identification

Efficiency in the identification of leptons depended on the energy as well as whether they occur in the barrel or endcap regions. For electrons in the barrel region, this was 1% below 90 GeV, 2% below 1 TeV, and 3% above 1 TeV. For electrons in the endcap region, this was 1% below 90 GeV, 2% below 300 GeV, and 4% above 400 GeV [62]. For muons, 1% was added for identification, another 0.5% for isolation, and another 0.5% for triggering [63].

Missing Transverse Energy

Uncertainties in MET were affected by both jet and lepton uncertainties, however, the MET uncertainties listed in Table 8.1 only refer to those that arise from "unclustered" energy deposits [64], arising from the energy deposits not associated with any reconstructed particle flow candidate.

Table 8.1 lists all of the normalization uncertainties in each process. In addition, before placing angular selections, most of the uncertainties listed in Table 8.1 were varied in order to achieve an uncertainty on the shape parameters. This uncertainty was propagated into the signal region via the alpha fit function. This procedure was not done after placing angular selections. The reason for this is that several angular selections were placed, meaning that the simulation had to be run multiple times. Additional running with varied values in order to compute uncertainty would have multiplied the computing time necessary. Instead, it was assumed that uncertainty on the shape parameters was unchanged. The errors on the shape parameters are given in Tables 8.2 to 8.5.

Table 8.1: Sources of normalization uncertainty in the analysis (%), listed by channel and process.

channel	electron				muon			
source	$t\bar{t}$	s-top	WW	WZ	$t\bar{t}$	s-top	WW	WZ
PDF	2.79	0.22	1.93	2.44	2.71	0.25	1.78	2.54
renorm/factor	17.99	0.94	5.77	4.82	17.74	1.06	5.99	4.26
lumi	2.5	2.5	2.5	2.5	2.5	2.5	2.5	2.5
pileup	0.59	0.29	0.90	1.40	0.40	0.41	0.82	0.67
τ_{21}	14	14	14	14	14	14	14	14
b-tag	1.05	0.85	0.04	0.08	1.04	0.84	0.03	0.08
b-mistag	0.04	0.05	0.02	0.04	0.05	0.05	0.03	0.04
JES	4.41	4.94	4.26	2.44	3.54	2.97	3.75	2.50
JER	1.79	3.44	1.85	2.69	0.85	0.91	0.62	2.92
LES	0.80	1.45	1.53	0.94	0.68	1.14	1.72	1.19
LER	0.26	1.22	0.11	0.21	0.02	0.27	0.14	0.33
lepID	2.12	2.22	2.30	2.26	1.81	2.04	2.55	2.42
MET	0.91	1.50	1.01	0.64	0.59	0.99	0.24	0.17
Total	23.74	15.84	16.44	15.91	23.30	14.85	16.31	15.80

Table 8.2: Uncertainties in the shape parameters for WW events in the electron channel.

param	PDF	ren/fac	PU	b-tag	b-mistag	JEC	JER	LEC	LER	lepID	MET
a_{cwww}	3.62	3.06	0.19	0.01	0.00	0.77	1.32	0.14	0.13	1.20	0.51
a_{cw}	2.84	2.76	0.19	0.01	0.00	1.06	0.83	0.46	0.25	1.02	0.21
a_{cb}	1.63	2.47	0.15	0.01	0.00	0.28	0.80	0.45	0.32	1.13	0.47

Table 8.3: Uncertainties in the shape parameters for WW events in the muon channel.

param	PDF	ren/fac	PU	b-tag	b-mistag	JEC	JER	LEC	LER	lepID	MET
a_{cwww}	4.47	1.88	0.33	0.01	0.01	0.54	1.21	1.34	0.13	0.28	1.01
a_{cw}	4.76	1.59	0.27	0.01	0.01	0.47	0.42	0.59	0.42	0.51	0.26
a_{cb}	1.40	1.45	0.18	0.01	0.00	0.39	0.07	0.19	0.07	0.50	0.08

Table 8.4: Uncertainties in the shape parameters for WZ events in the electron channel.

param	PDF	ren/fac	PU	b-tag	b-mistag	JEC	JER	LEC	LER	lepID	MET
a_{cwww}	5.86	2.46	0.37	0.00	0.01	1.26	0.60	0.50	0.35	1.18	0.54
a_{cw}	4.81	2.12	0.56	0.00	0.01	2.02	0.82	0.67	0.05	0.92	0.06
a_{cb}	2.57	2.35	0.31	0.01	0.00	2.85	1.97	0.81	0.31	1.07	0.33

Table 8.5: Uncertainties in the shape parameters for WZ events in the muon channel.

param	PDF	ren/fac	PU	b-tag	b-mistag	JEC	JER	LEC	LER	lepID	MET
a_{cwww}	3.60	2.22	0.08	0.00	0.01	2.02	0.51	1.34	0.38	0.23	0.31
a_{cw}	2.98	1.18	0.23	0.01	0.01	2.12	1.21	0.60	0.47	0.46	0.37
a_{cb}	2.21	2.71	0.26	0.00	0.01	3.04	0.26	0.81	0.75	0.51	0.85

CHAPTER 9 RESULTS

To compute the final limits on the anomalous couplings, the Higgs Combine Tool [65] was used. After the background and signal distributions were modeled, limits were set at the 95% confidence level on the anomalous parameters using delta log-likelihood. The modeling of signal, both standard model and anomalous couplings, can be seen before any angular selections [30] in Figures 9.1 and 9.2. After an angular selection of $|\cos\theta^*| < 0.8$ was placed on the data and Monte Carlo, the same modeling can be seen in Figures 9.3 and 9.4.

One-dimensional limits were computed by setting two of the three anomalous parameters to zero, and varying the third. Two-dimensional limits were also computed by allowing two to vary and keeping the third fixed to 0. According to Wilk's Theorem [66], ΔNLL distributions tend to χ^2 distributions as the number of data points tends to infinity, with the number of degrees of freedom depending on the number of free parameters (Two degrees of freedom for the two-dimensional limits, one degree of freedom for the one-dimensional limits). For the one-dimensional limits, a 95% confidence level corresponds to a χ^2 value of 3.84, while for the two-dimensional limits, the same confidence level corresponds to a value of 5.99. The value can then be projected onto the parameter axis to determine the values of the limits. Both observed and expected limits were calculated. The expected limits were calculated using Asimov data normalized to the expected yield. (Asimov data refers to a data set generated by taking the expectation value of a data set, and varying it to generate a larger data set for computing an expected limit.) Limits were found using a simultaneous unbinned maximum likelihood fit. The best fit values of the anomalous parameters, as well as their confidence intervals, were obtained using scans of the profile likelihood ratio, as described in Section 3.2 of Ref. [67].

The sensitivity to anomalous couplings in angular distributions is illustrated by plotting the angular distributions of the standard model couplings as well as for nonzero values of the anomalous couplings for signal MC. The plots in Figure 9.5 show the results for $\cos\theta^*$ with the standard model value along with the smaller positive and negative values of each coupling

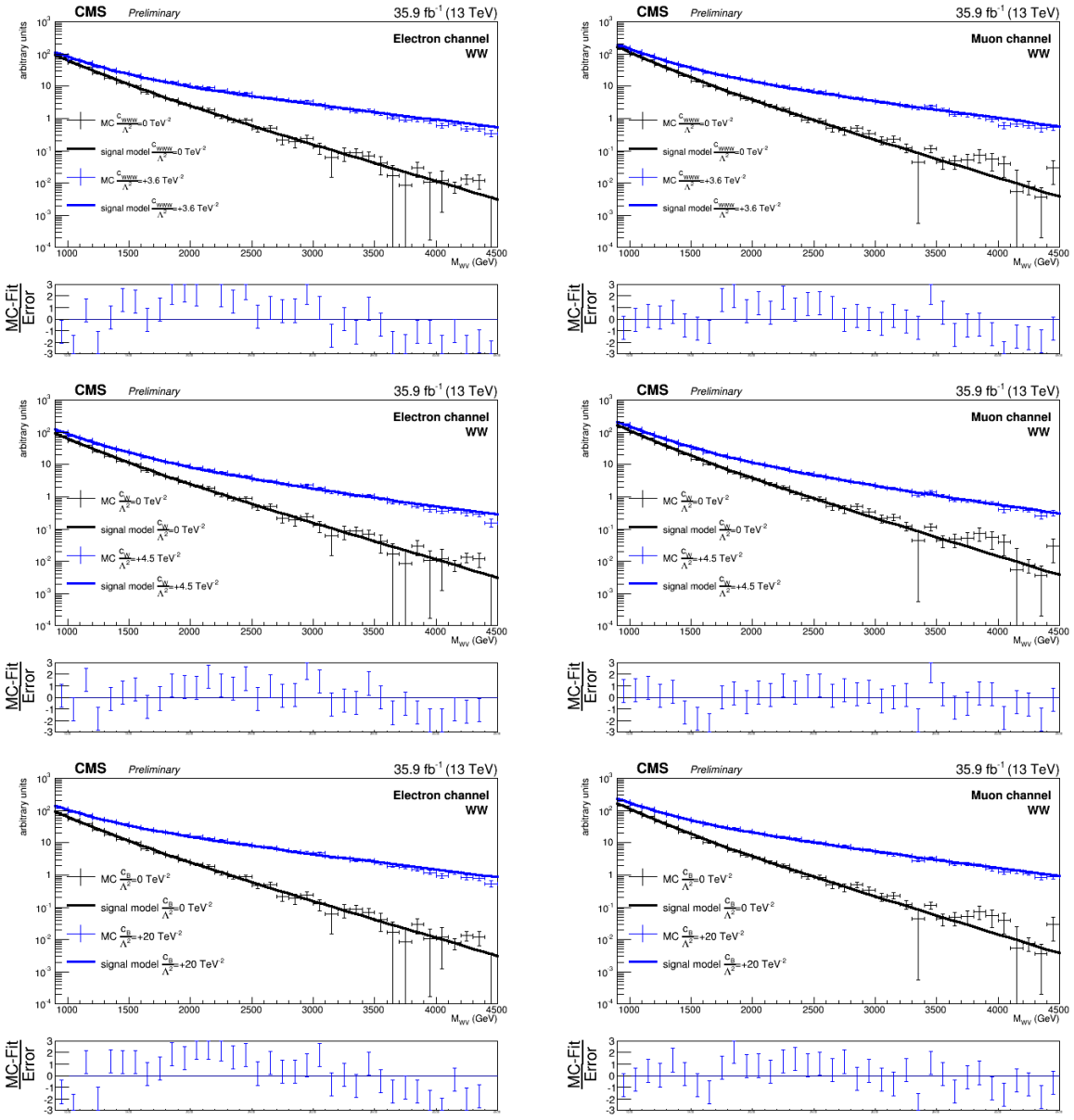

Figure 9.1: Equation 7.2 was used to model signal Monte Carlo in the standard model (black) compared with anomalous couplings. Shown is WW events, electron channel on left, muon channel on right. Top is the c_{WWW}/Λ^2 parameter, middle is the c_W/Λ^2 parameter, and bottom is the c_B/Λ^2 parameter. All plots are before angular selections. Positive values for the parameters are shown. Negative values give similar results.

given in Table 6.1, and clearly show sensitivity to the changes in anomalous couplings.

Note that the anomalous couplings cause more events to occur at the lower absolute values of the cosines of the angles. The bump seen in the middle of the histograms is a result

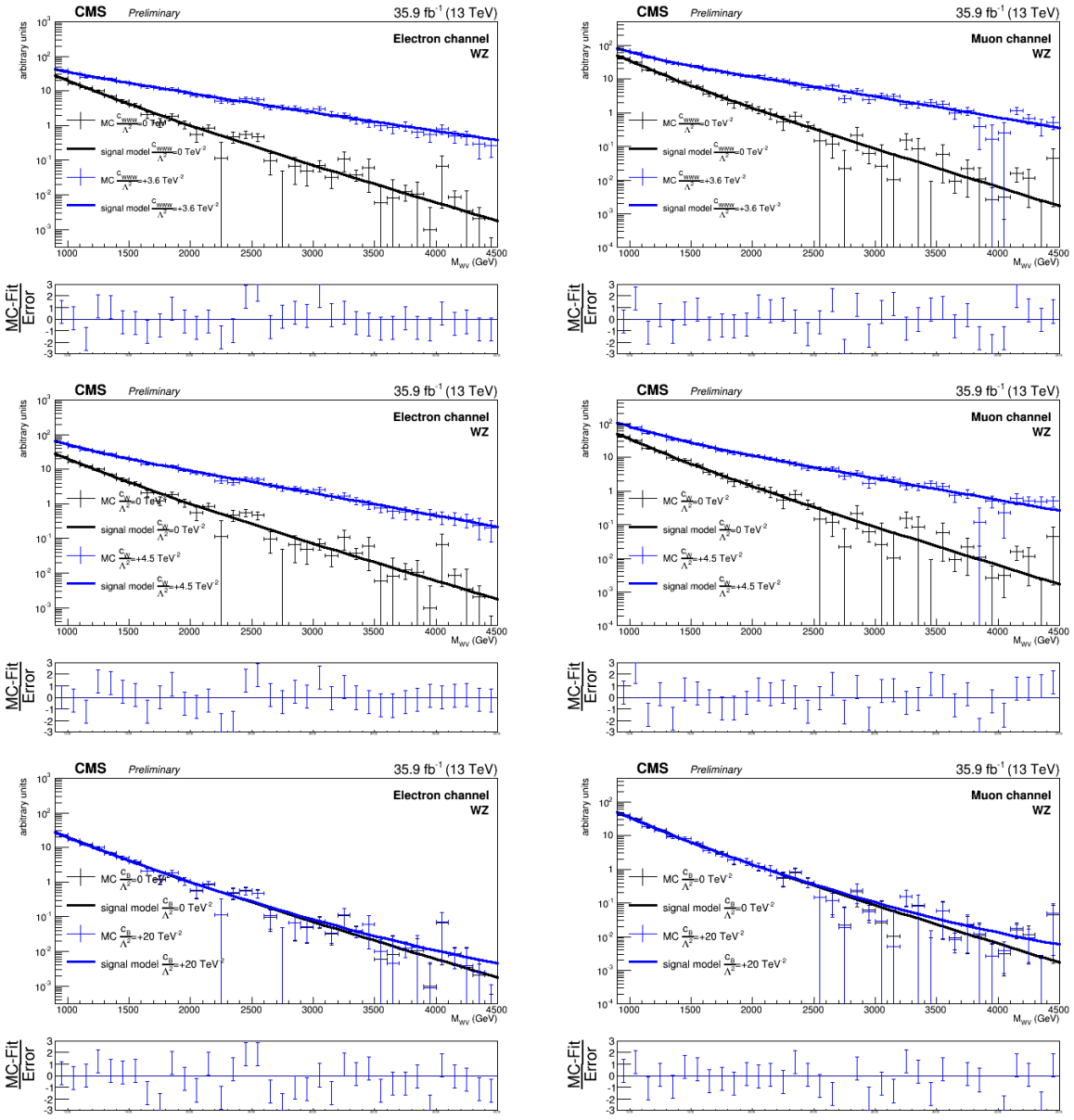

Figure 9.2: Equation 7.2 was used to model signal Monte Carlo in the standard model (black) compared with anomalous couplings. Shown is WZ events, electron channel on left, muon channel on right. Top is the c_{WWW}/Λ^2 parameter, middle is the c_W/Λ^2 parameter, and bottom is the c_B/Λ^2 parameter. All plots are before angular selections. Positive values for the parameters are shown. Negative values give similar results.

of selecting the wrong neutrino p_z, as explained in Section 5.4.2. The c_W/Λ^2 parameter is the only one of the three that show asymmetric limits with respect to the distribution of cos θ^*. Other angles were explored for sensitivity to anomalous couplings, but did not show

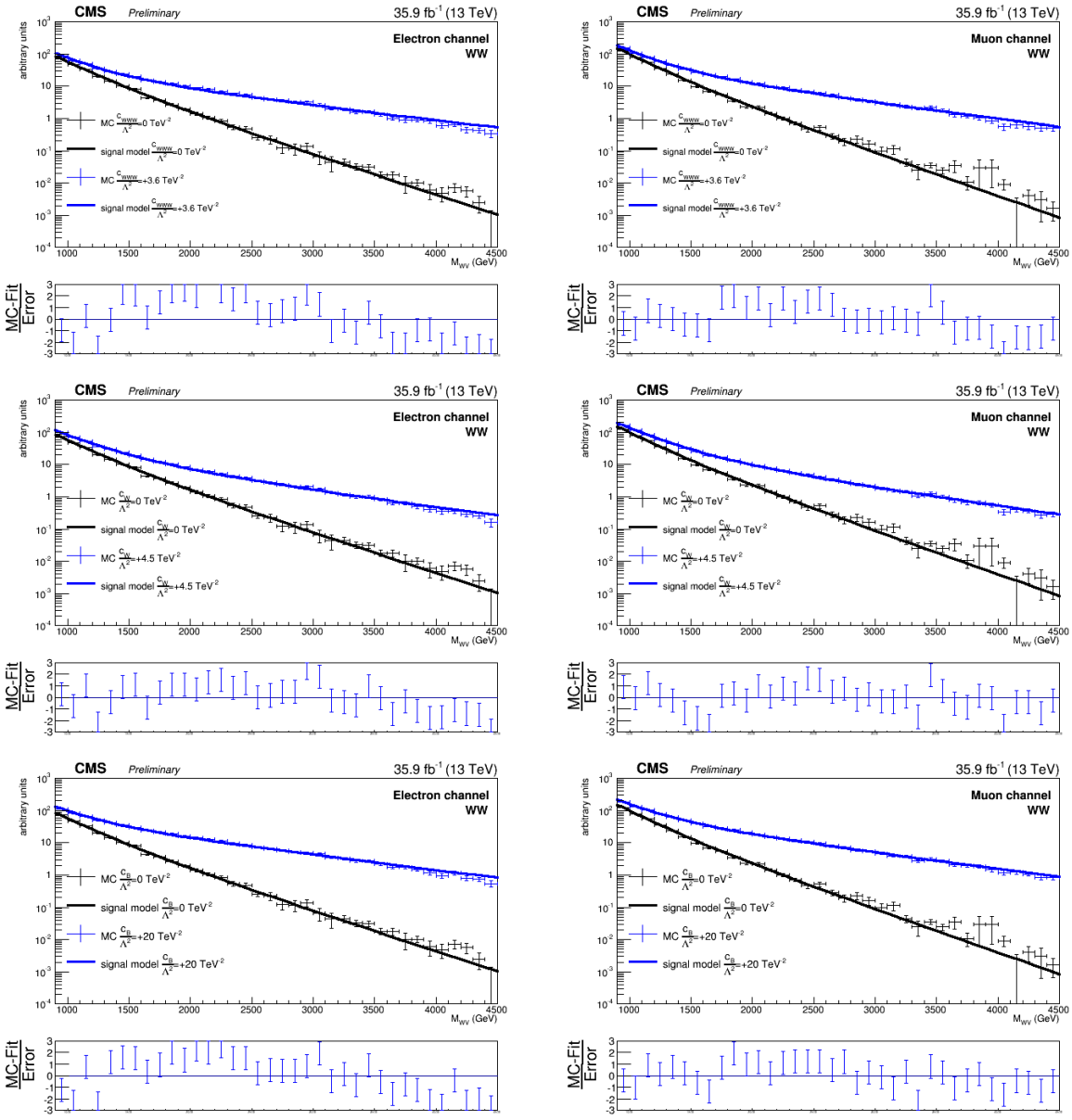

Figure 9.3: Equation 7.2 was used to model signal Monte Carlo after an angular selection of $|\cos\theta^*| < 0.8$ in the standard model (black) compared with anomalous couplings. Shown is WW events, electron channel on left, muon channel on right. Top is the c_{WWW}/Λ^2 parameter, middle is the c_W/Λ^2 parameter, and bottom is the c_B/Λ^2 parameter. Positive values for the parameters are shown. Negative values give similar results.

significant sensitivity, as can be seen in Figures 9.6 and 9.7. The angles Φ, Φ_1, and Φ_2 are not shown, but showed flat behavior for standard model and anomalous signal, as well as for background.

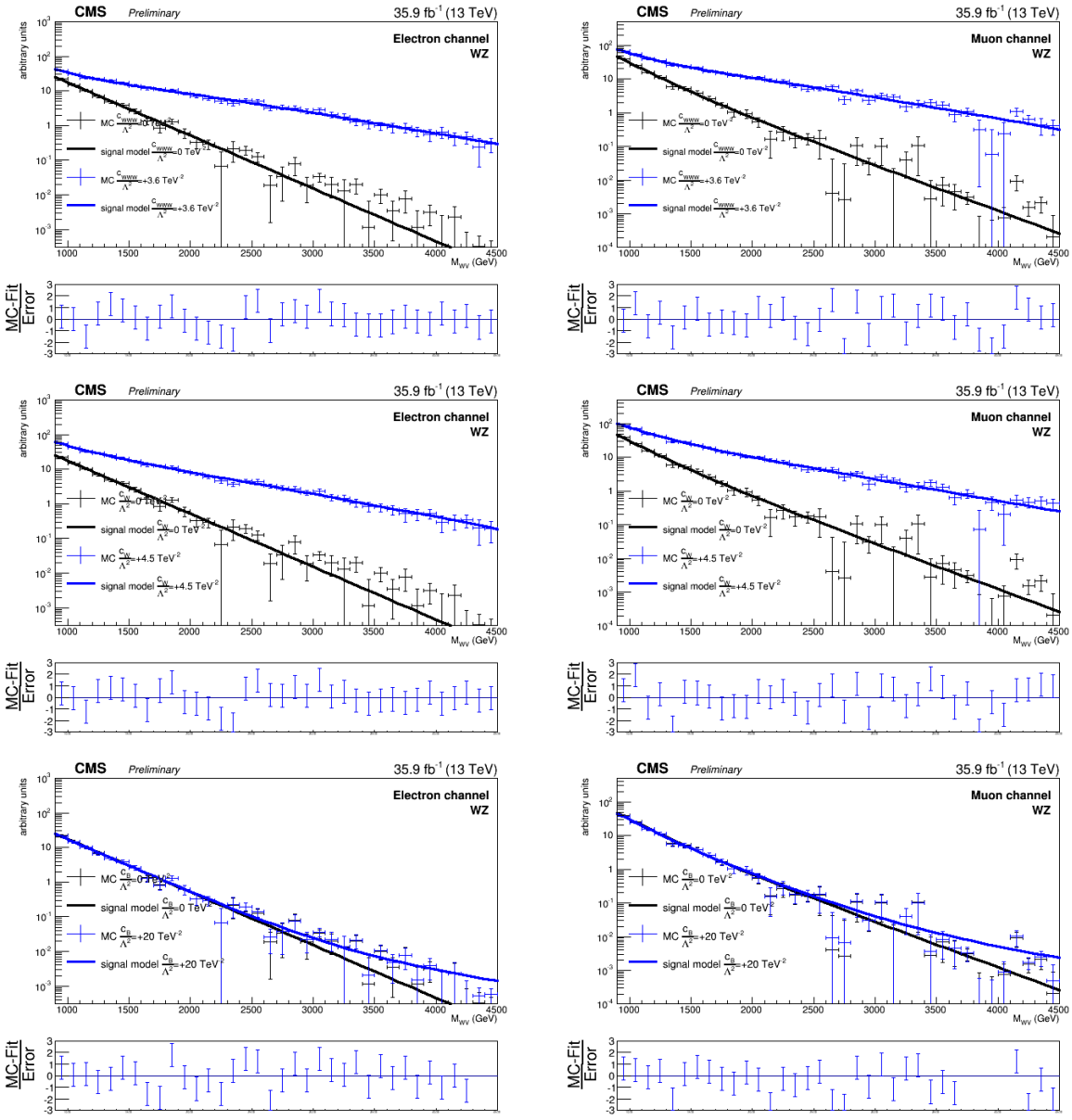

Figure 9.4: Equation 7.2 was used to model signal Monte Carlo after an angular selection of $|\cos\theta^*| < 0.8$ in the standard model (black) compared with anomalous couplings. Shown is WZ events, electron channel on left, muon channel on right. Top is the c_{WWW}/Λ^2 parameter, middle is the c_W/Λ^2 parameter, and bottom is the c_B/Λ^2 parameter. Positive values for the parameters are shown. Negative values give similar results.

Note that these plots are normalized to unit area in order to highlight the shape difference, while factoring out differences in the overall cross section.

Looking now at the angular distributions of signal versus background (normalized to

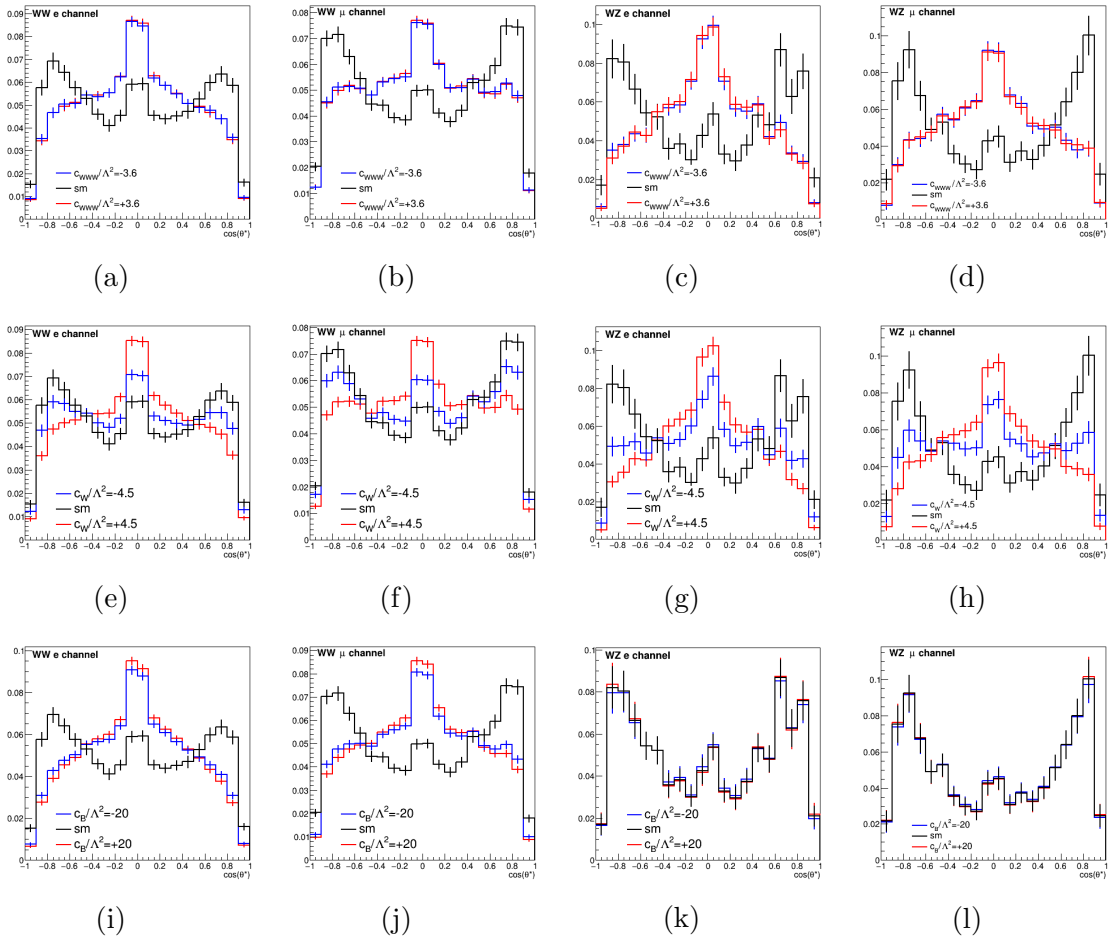

Figure 9.5: The distributions for cos θ^* show sensitivity to the anomalous couplings. Anomalous parameters show a markedly different shape.

unit area), it can also be seen in Figure 9.8 that $\cos\theta^*$, along with $\cos\theta_1$ and $\cos\theta_2$, shows sensitivity to signal versus background. In Figure 9.8, the primary signal Monte Carlo, WW, is in black whereas the primary background Monte Carlo, W+jets, is in red.

Looking at $\cos\theta_1$ (left), the W+jets background is biased towards positive values of the cosine, whereas signal and other backgrounds are symmetrical between positive and negative values. All backgrounds tend to more central values of $\cos\theta_1$, peaking at either the center, or to right in the case of W+jets. The signal, by contrast, has more of a flat shape through the center. Looking at $\cos\theta_2$ (middle), the the shape of the W+jets distribution is noticeably different from the signal. There does not appear to be much discriminating power for the

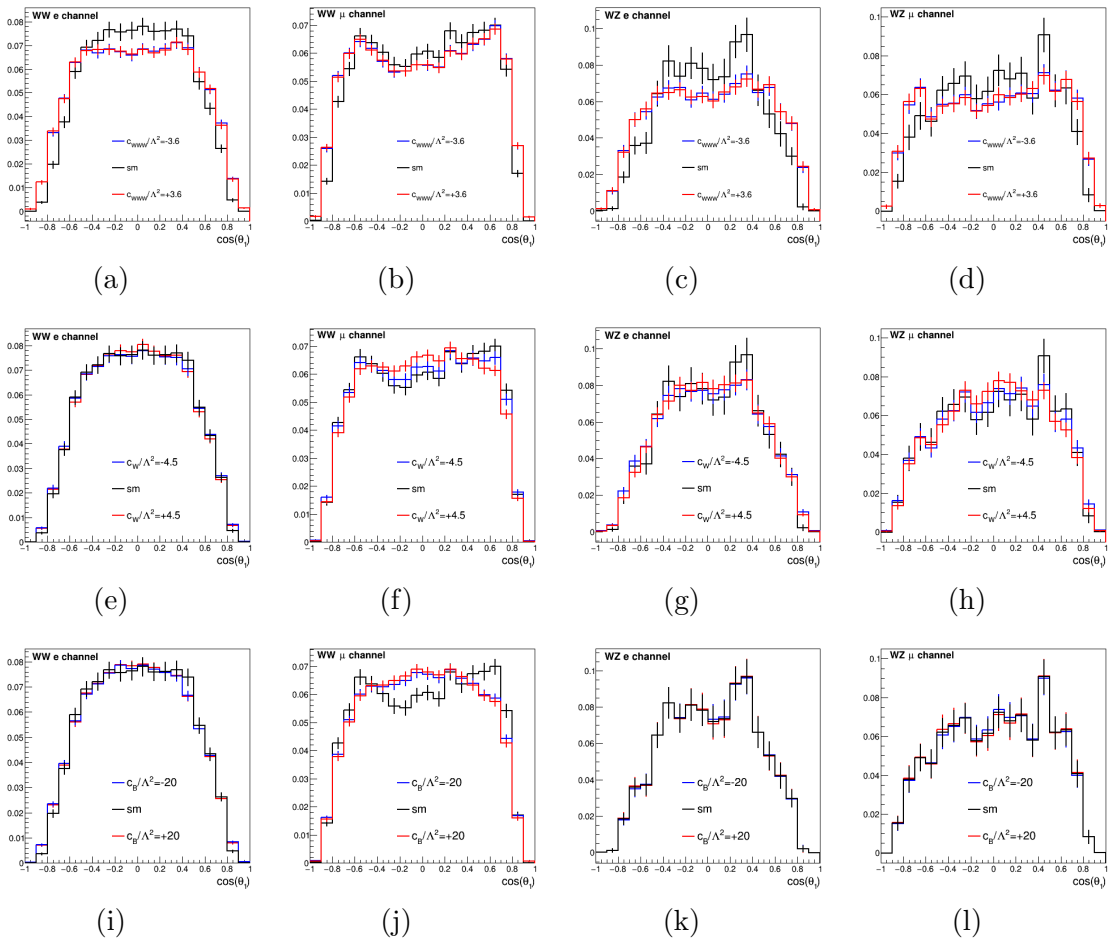

Figure 9.6: The distribution of cos θ_1 shows no significant distinction between standard model and anomalous couplings.

$t\bar{t}$ or single top background from this angle, but the W+jets was the primary background. Finally, looking at the distributions of cos θ^* (right), we see that all of the backgrounds are biased toward the higher absolute values of the angle, while the signal is biased towards the lower absolute values.

The fitting functions that were described in Chapter 7 had to be slightly modified for the W+jets background when applying angular cuts for cos θ^*, though not for cos θ_1. There was only one selection applied to cos θ_1, which showed an improvement in observed but not expected limits. There are no limits shown with a selection on cos θ_2, because there was not a fitting function that could be found to properly fit the shape.

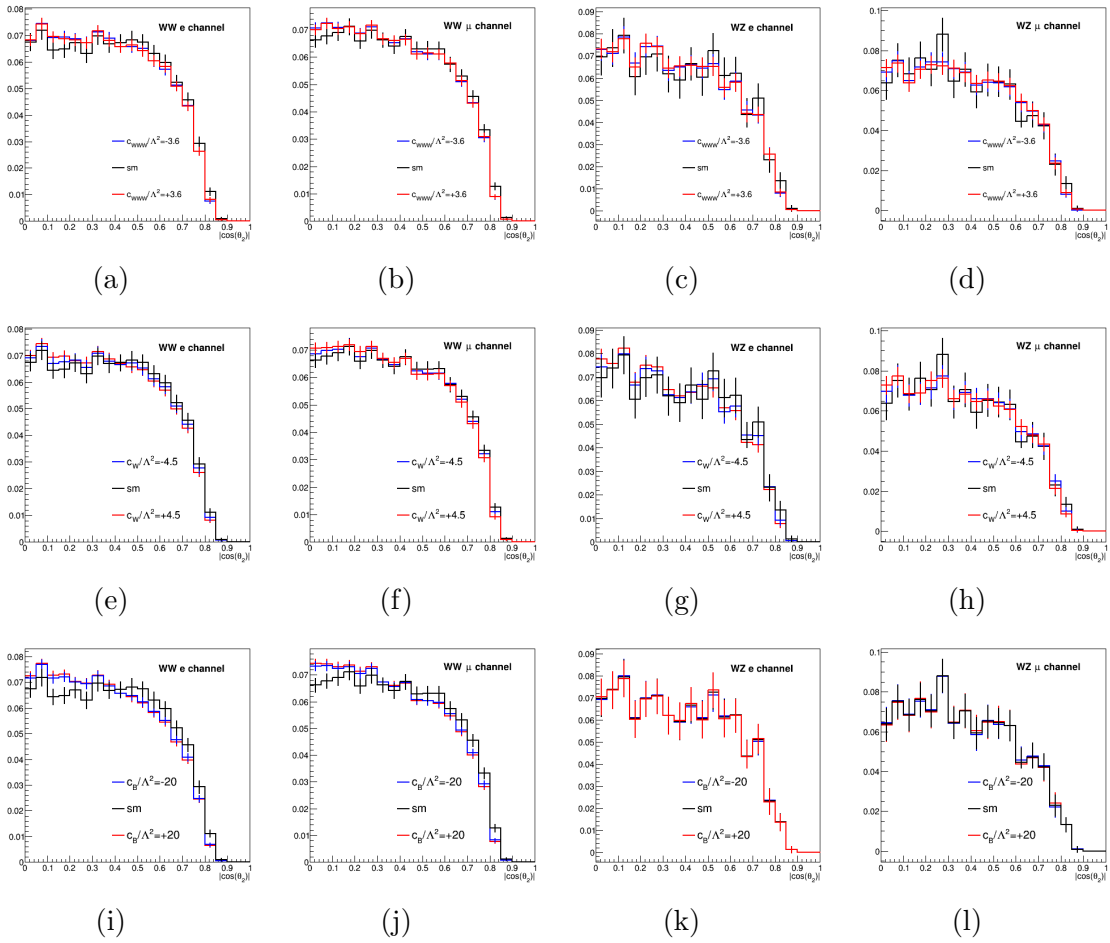

Figure 9.7: The distribution of $|\cos\theta_2|$ shows no significant distinction between standard model and anomalous couplings.

The results of fitting, prior to any angular selections being applied, can be seen in Figures 9.9 - 9.13. Each figure shows Monte Carlo events for a specified process, and the function that was fit to those events in the signal and background regions. All of the events together, in a stacked plot, can be seen in Figure 9.14, to see the final overall fit after the unblinding.

After applying the angular selections, it was observed that the W+jets background did not fit well with Equation 7.3, as can be seen in the left of Figure 9.15 for the muon channel in the signal region of the W+jets, with an angular cut of $\cos\theta^*$ less than 0.8. After replacing Equation 7.3 with Equation 7.4, the improved plot can be seen in the right of Figure 9.15.

Various selections were placed on the values of the cosines of two of the angular variables,

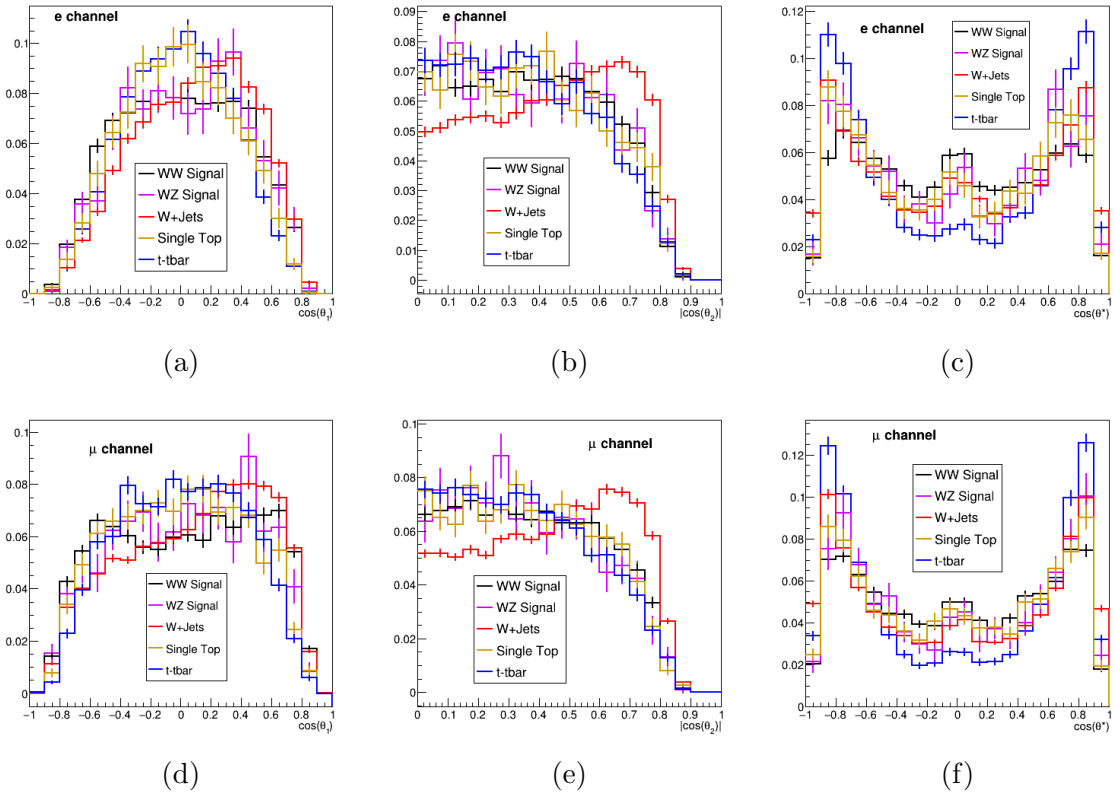

Figure 9.8: Distributions of angles for signal processes versus the various background processes. The major backgrounds of W+jets (red) and $t\bar{t}$ (blue) compared to the primary signal (black), all normalized to unit area.

$\cos\theta^*$ and $\cos\theta_1$, in order to see what the effect was on the anomalous coupling limits. Figure 9.16, which comes from the published CMS results of the same data [30] shows the one- and two-dimensional limits on the anomalous couplings before angular selections were applied. All of these are delta log likelihood limits, as described earlier in this chapter. The one-dimensional limits on each coupling were calculated assuming the other two couplings to be zero. The green curve represents the expected limits, which corresponds to 95% confidence at the point where it intersects the dashed green vertical bar. The points where the curve intersects the dashed red and blue bars represent the 99% and 68% confidence levels, respectively. The black curve represents the observed limits, where the intersection of the curve with the black vertical dashed line represents the 95% confidence level. The two-dimensional limits vary two couplings at a time, assuming the third to be zero. The

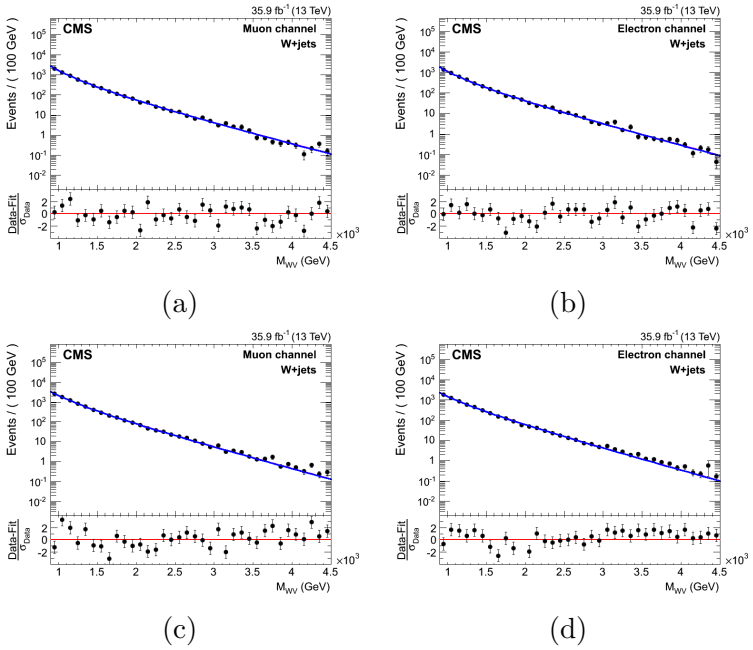

Figure 9.9: Fitting for W+jets background MC events, on a log scale, prior to any angular selections. Signal region (top) and W+jets control region (bottom). Muon channel (left) and electron channel (right).

solid black curve in the 2D plots represents the observed 95% confidence level, while the dashed red, green, and blue curves represent the expected 99%, 95%, and 68% confidence levels, respectively. The thick black cross in the 2D plots represents the best-fit point in the Asimov data, while the thick square represents the standard model point with both couplings at 0. The top of Table 9.1 shows the limits placed on the anomalous couplings prior to any angular selections.

Placing a selection of cosine of θ^* less than 0.5 gave improvement, with a 30% increase on the c_{WWW} parameter, and a 25% and 35% increase on the lower and upper bounds, respectively, of the c_B parameter, as seen in Figure 9.17 as well as Table 9.1. The improvement of the observed limits of the c_W parameter were more dramatic, with a 64% increase on the upper limit for the selection of 0.5, but only a 4% increase for the lower limit. Increasing the maximum value from 0.5 to 0.6 showed a slight degradation in all of the observed limits, as can be seen in Figure 9.18, and a value of 0.7 showed little change from 0.6, as seen

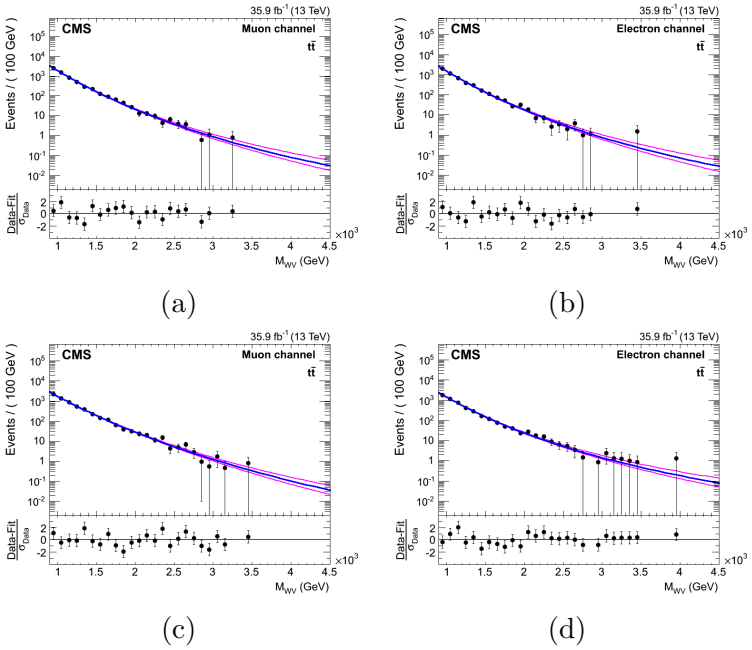

Figure 9.10: Fitting for $t\bar{t}$ background MC events, on a log scale, prior to any angular selections. Signal region (top) and $t\bar{t}$ control region (bottom). Muon channel (left) and electron channel (right).

in Figure 9.19. Setting the selection on the cosine of θ^* to 0.8 made the limits on c_W/Λ^2 more symmetric, with a 4% improvement over no selection. The limits on c_{WWW}/Λ^2 did not appreciably change, while the limits on c_B/Λ^2 degraded a bit, with only a 12% improvement in observed limits, as seen in Figure 9.20. For the selections on the cosine of the θ_1 angle less than 0.6, more modest improvements were gained as seen in Figure 9.21, with about a 6% improvement on the c_{WWW}/Λ^2 parameter, and a 12% improvement on the c_B/Λ^2 parameter.

As in the case of the selection on cos θ_1, the observed limits on the c_W/Λ^2 parameter improved asymmetrically, with a larger improvement on the upper limits of 12%, though not as dramatic of a difference. The improvements on the lower limits of c_W/Λ^2 were actually slightly better with the selection on cos θ_1, at 5%.

These results are significant. If we expect limits to improve proportionally to $\frac{1}{\sqrt{N}}$, where N is number of events, a 30% improvement corresponds to roughly a doubling of statistics.

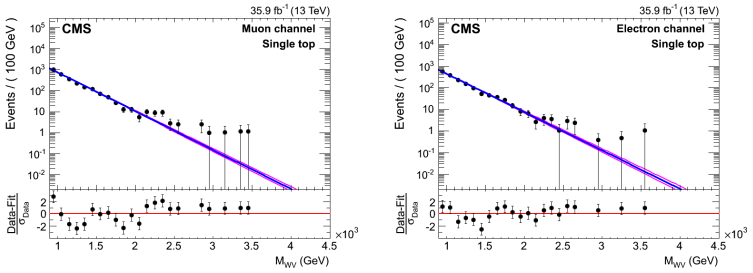

(a)

(b)

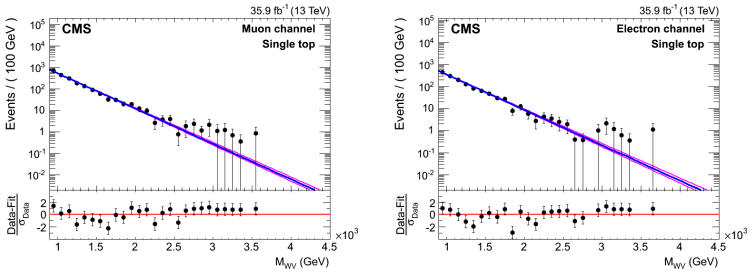

(c)

(d)

Figure 9.11: Fitting for single top background MC events, on a log scale, prior to any angular selections. Signal region (top) and w+jets control region (bottom). Muon channel (left) and electron channel (right).

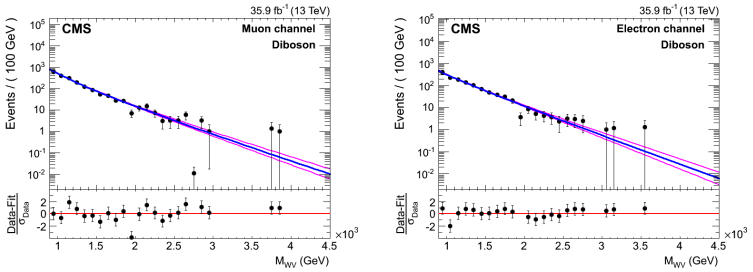

(a)

(b)

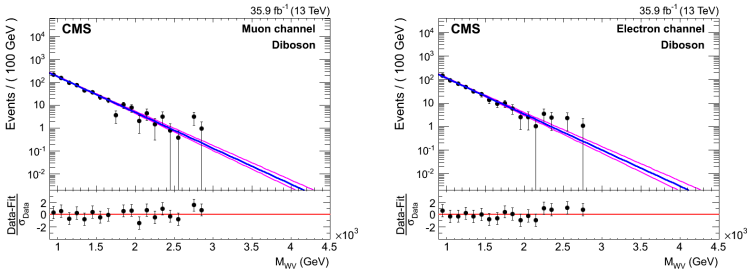

(c)

(d)

Figure 9.12: Fitting for standard model WW signal MC events, on a log scale, prior to any angular selections. Signal region (top) and W+jets control region (bottom). Muon channel (left) and electron channel (right).

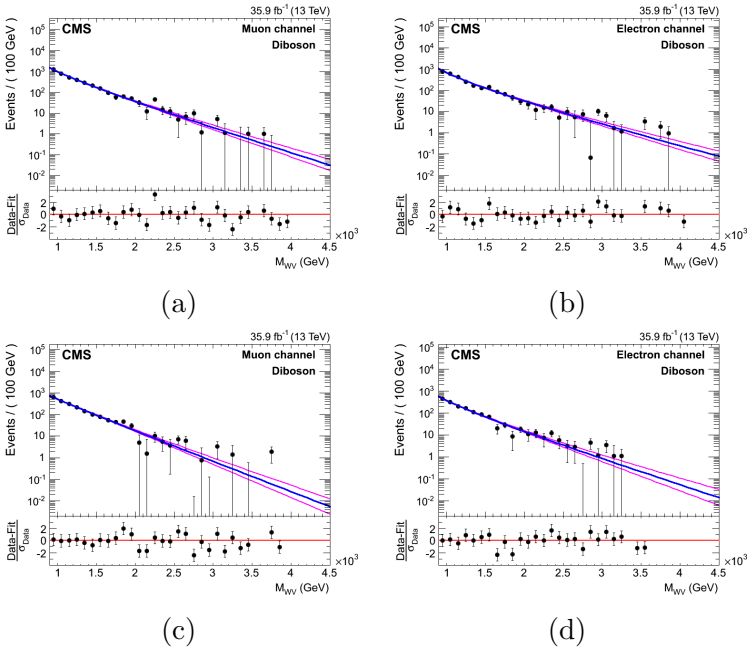

Figure 9.13: Fitting for standard model WZ signal MC events, on a log scale, prior to any angular selections. Signal region (top) and W+ jets control region (bottom). Muon channel (left) and electron channel (right).

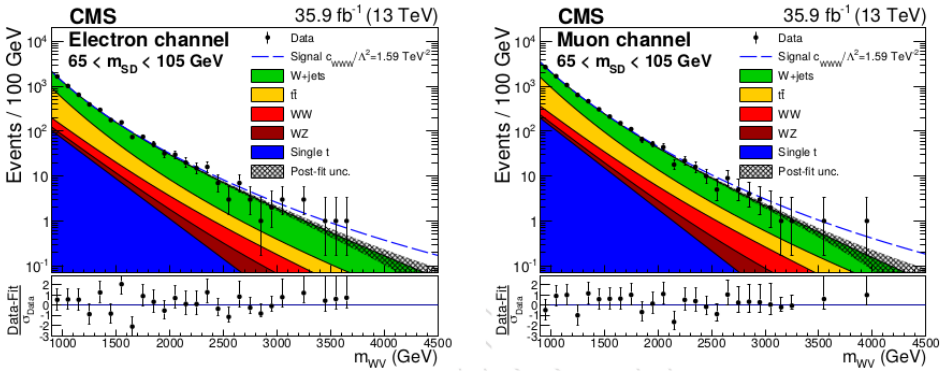

Figure 9.14: All of the Monte Carlo together in the signal region, along with the data after unblinding, before any angular selections were added. Electron channel (left) and muon channel (right).

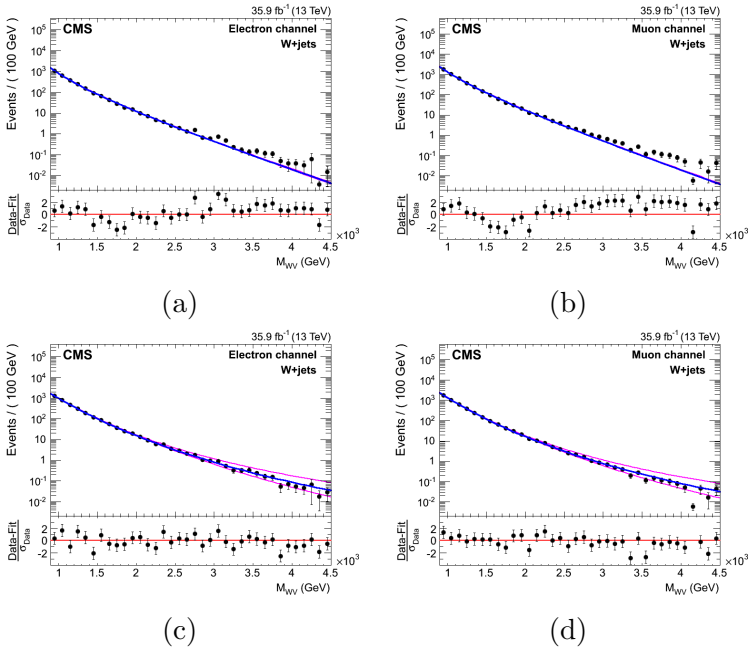

Figure 9.15: W+jets fitting in the muon channel before (top) and after (bottom) W+jets equation was modified. Electron channel on left, muon channel on right.

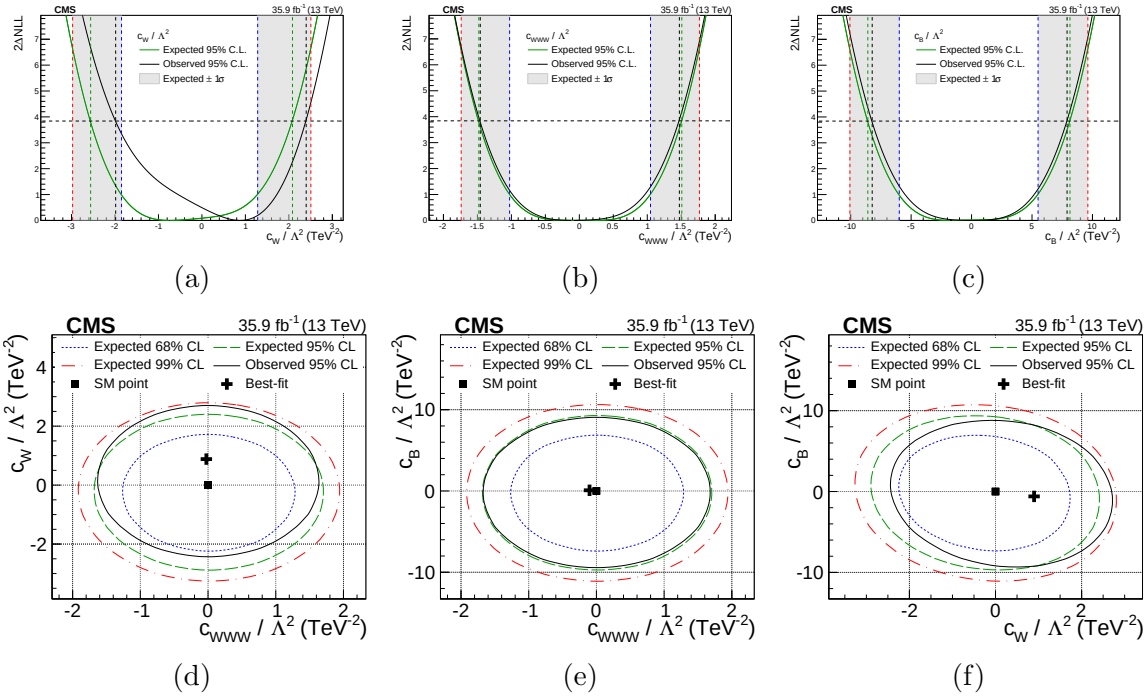

Figure 9.16: Limits on the anomalous parameters before the angular selections were applied. Expected limits shown in blue (68% confidence), green (95% confidence), and red (99% confidence). Observed limits shown in black (95% confidence).

Table 9.1: Limits on anomalous couplings before [30] and after angular selections were added. Expected limits are from simulation, observed limits are from data. All limits from angular cuts are new, and have not been published.

aTGC (TeV^{-2})	Expected limit (sim)	Observed limit (data)
prior to selection		
c_{WWW}/Λ^2	[-1.44,+1.47]	[-1.58,+1.59]
c_W/Λ^2	[-2.45,+2.08]	[-2.00,+2.65]
c_B/Λ^2	[-8.38,+8.06]	[-8.78,+8.54]
selection of $\lvert\cos\theta^*\rvert < 0.5$		
c_{WWW}/Λ^2	[-0.918,+0.932]	[-1.05,+1.08]
c_W/Λ^2	[-1.60,+1.29]	[-1.92,+0.967]
c_B/Λ^2	[-5.62,+5.22]	[-6.58,+5.38]
selection of $\lvert\cos\theta^*\rvert < 0.6$		
c_{WWW}/Λ^2	[-0.911,+0.925]	[-1.08,+1.11]
c_W/Λ^2	[-1.58,+1.28]	[-1.93,+1.17]
c_B/Λ^2	[-5.54,+5.18]	[-6.54,+5.38]
selection of $\lvert\cos\theta^*\rvert < 0.7$		
c_{WWW}/Λ^2	[-0.911,+0.925]	[-1.09,+1.11]
c_W/Λ^2	[-1.58,+1.28]	[-1.92,+1.35]
c_B/Λ^2	[-5.46,+5.14]	[-6.58,+5.58]
selection of $\lvert\cos\theta^*\rvert < 0.8$		
c_{WWW}/Λ^2	[-1.11,+1.13]	[-1.02,+1.03]
c_W/Λ^2	[-1.95,+1.54]	[-1.66,+1.51]
c_B/Λ^2	[-6.58,+6.14]	[-6.10,+5.42]
selection of $\lvert\cos\theta_1\rvert < 0.6$		
c_{WWW}/Λ^2	[-1.57,+1.60]	[-1.47,+1.48]
c_W/Λ^2	[-2.59,+2.12]	[-1.89,+2.34]
c_B/Λ^2	[-8.66,+8.22]	[-7.74,+7.42]
selection of $\lvert\cos\theta_2\rvert < 0.6$		
c_{WWW}/Λ^2	[-1.52,+1.55]	[-1.29,+1.30]
c_W/Λ^2	[-2.61,+2.15]	[-2.01,+2.05]
c_B/Λ^2	[-8.62,+8.18]	[-7.02,+6.38]

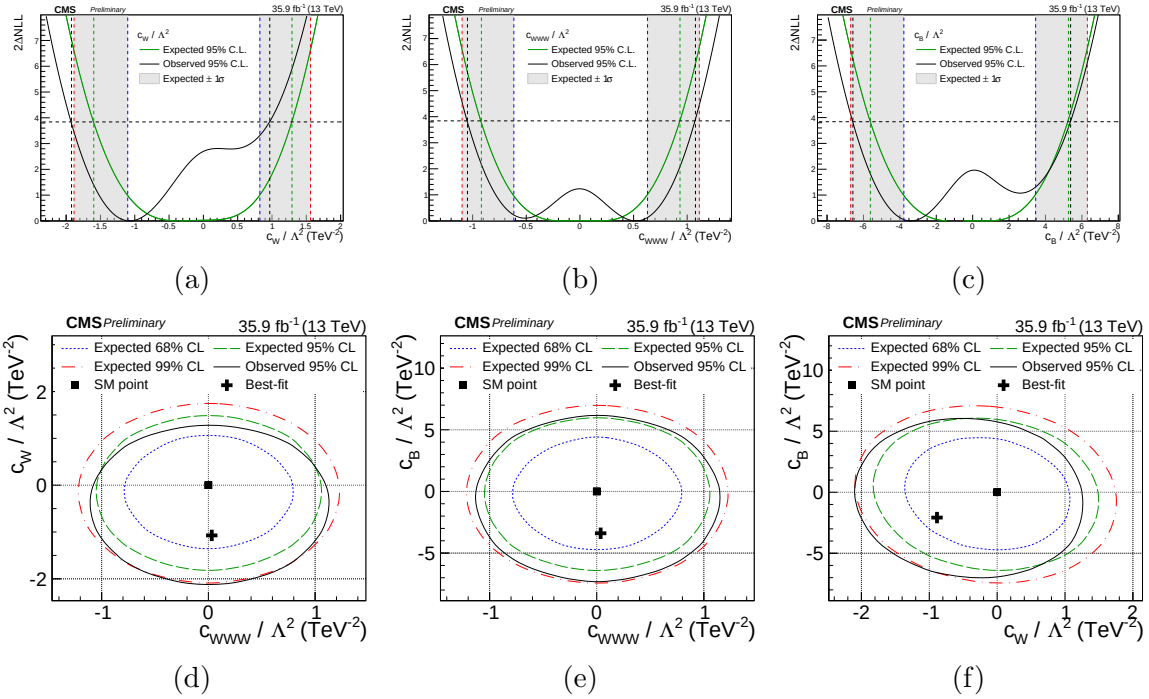

Figure 9.17: Limits on the anomalous parameters after an angular selection of $|\cos\theta^*| < 0.5$ was applied. Expected limits shown in blue (68% confidence), green (95% confidence), and red (99% confidence). Observed limits shown in black (95% confidence).

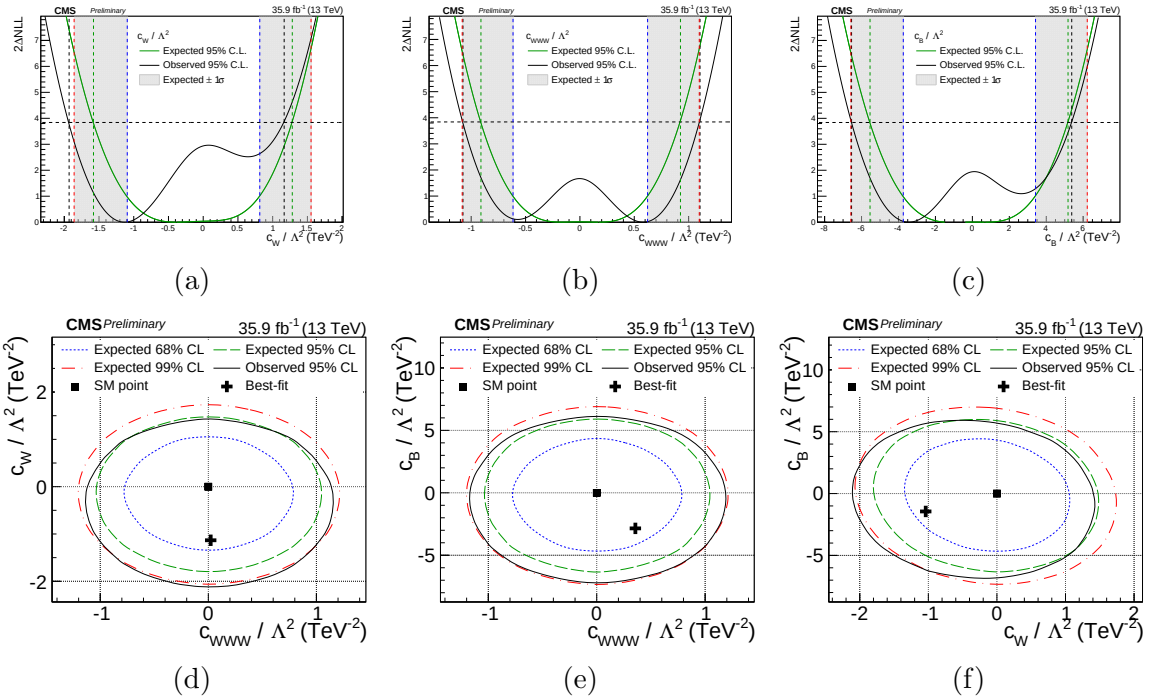

Figure 9.18: Limits on the anomalous parameters after an angular selection of $|\cos\theta^*| < 0.6$ was applied. Expected limits shown in blue (68% confidence), green (95% confidence), and red (99% confidence). Observed limits shown in black (95% confidence).

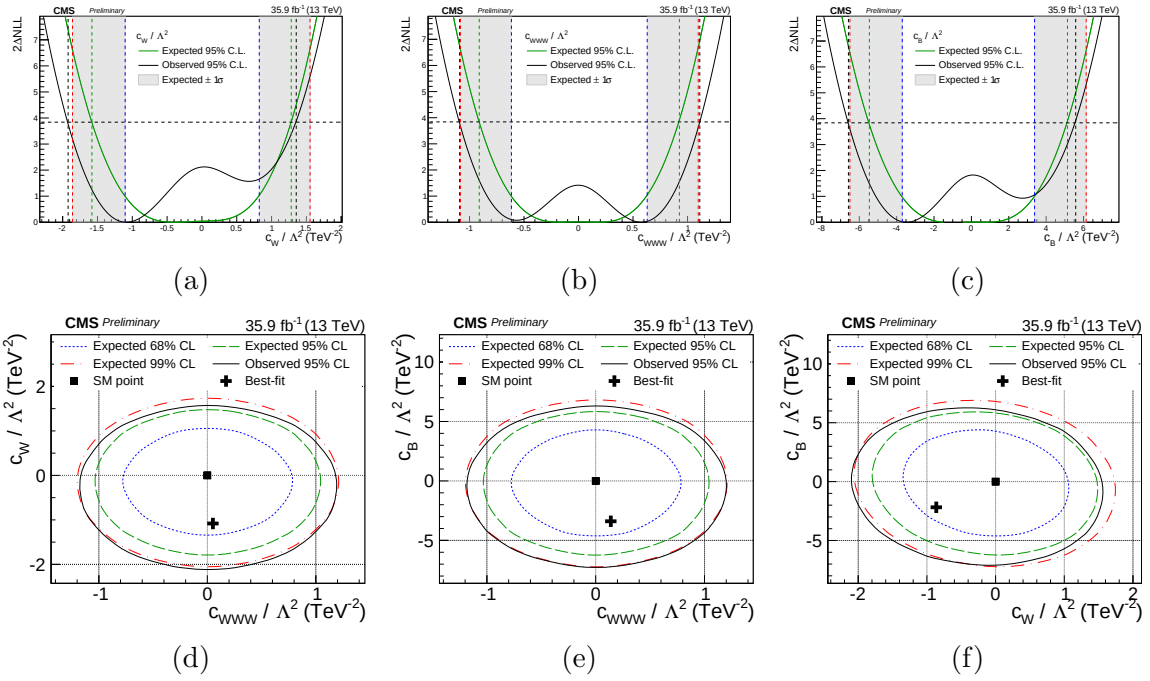

Figure 9.19: Limits on the anomalous parameters after an angular selection of $|\cos\theta^*| < 0.7$ was applied. Expected limits shown in blue (68% confidence), green (95% confidence), and red (99% confidence). Observed limits shown in black (95% confidence).

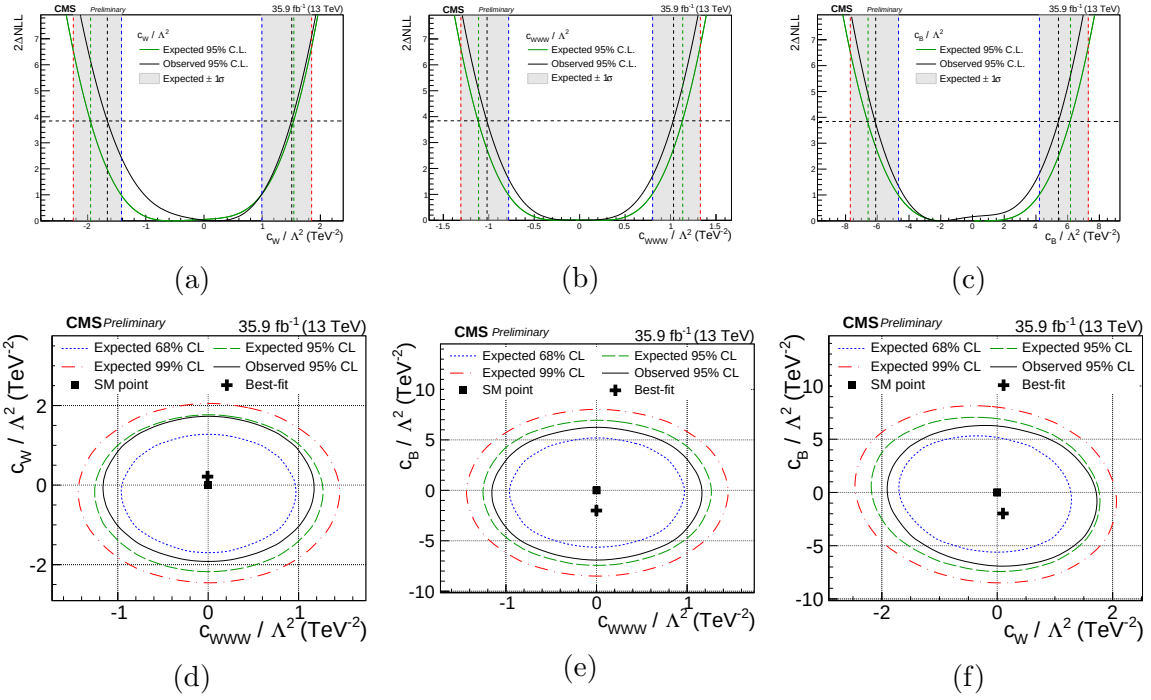

Figure 9.20: Limits on the anomalous parameters after an angular selection of $|\cos\theta^*| < 0.8$ was applied. Expected limits shown in blue (68% confidence), green (95% confidence), and red (99% confidence). Observed limits shown in black (95% confidence).

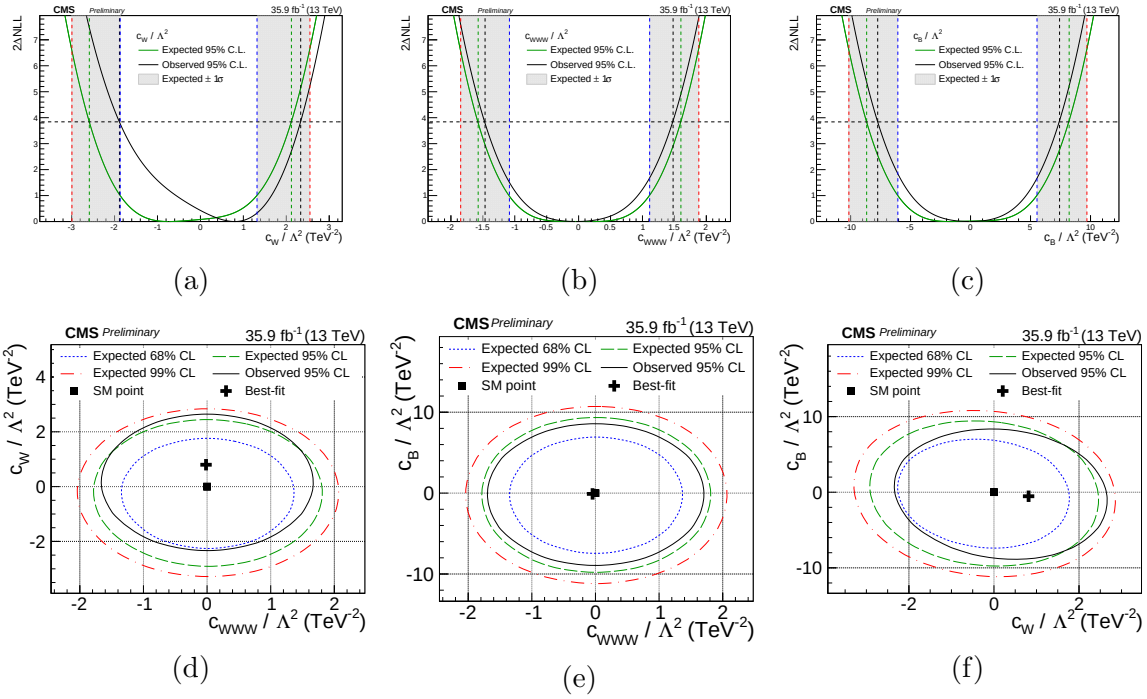

Figure 9.21: Limits on the anomalous parameters after an angular selection of $|\cos\theta_1| < 0.6$ was applied. Expected limits shown in blue (68% confidence), green (95% confidence), and red (99% confidence). Observed limits shown in black (95% confidence).

CHAPTER 10 CONCLUSIONS

This analysis has shown that angular variables can be used to improve limits placed on anomalous trilinear gauge couplings. While the resulting limits show an improvement based on selections of both $|\cos\theta^*|$ and $|\cos\theta_1|$, with optimal selection being around 0.8 for $|\cos\theta^*|$, more exploration is needed. Only one selection was attempted for $|\cos\theta_1|$, of 0.6, due to time constraints, which improved the observed limits, but not the expected limits. Placing selections on $|\cos\theta^*|$ required a modification of the fit function, replacing Equation 7.3 with Equation 7.4. On the other hand, Equation 7.3 worked when selections were placed on $|\cos\theta_1|$. Neither Equation 7.4 nor Equation 7.3 worked when a selection was placed on $|\cos\theta_2|$. The result of this was that expected and observed limits failed to converge. Investigation is needed to discover the correct fitting function for these selections. In addition, no attempt was made to place selections on more than one angular variable, which may prove useful.

Placing selections on the angular variables can increase the signal to background ratio, as well as provide sensitivity to the anomalous couplings. This appears to have led to an improvement of around 30% for limits on two of the three couplings, and an asymmetric improvement of 64% for the limits on the third. The 30% improvement corresponds roughly to a doubling of statistics, while a symmetric improvement of 64% would correspond to a whopping eight(!) times the statistics. It should be noted that these limits improve on those set by Reference [30], which are currently the best in the world. It should be pointed out that the 64% improvement for the c_B/Λ^2 parameter is not symmetric, and it is not understood why this is so. Uncertainties on the shape parameters were performed in Reference [30] by rerunning the simulation while varying PDFs and other inputs within their uncertainties, as explained in Chapter 8. Because this analysis already involved running the simulation multiple times, these uncertainties were not recalculated, so more work is needed to confirm these uncertainties.

This analysis has also shown the effectiveness of several methods of selecting from between

two values of neutrino p_z, with the most effective method for this analysis being to simply take the smaller absolute value. More work can be done to improve the selection method, such as the possibility of a combination of the methods already tried.

BIBLIOGRAPHY

[1] Sidney A. Bludman, N. Hata, D. C. Kennedy, and P. G. Langacker. Implications of combined solar neutrino observations and their theoretical uncertainties. *Phys. Rev.*, D47:2220–2233, 1993.

[2] B.R. Martin and G. Shaw. *Particle Physics*. Wiley, 1997.

[3] The elegant universe. `https://www.pbs.org/wgbh/nova/series/the-elegant-universe/`. PBS Broadcasting.

[4] H. David Politzer. Asymptotic Freedom: An Approach to Strong Interactions. *Phys. Rept.*, 14:129–180, 1974.

[5] Roel Aaij et al. Observation of $J/\psi\phi$ structures consistent with exotic states from amplitude analysis of $B^+ \to J/\psi\phi K^+$ decays. *Phys. Rev. Lett.*, 118(2):022003, 2017.

[6] Vernon D. Barger and Roger J.N. Phillips. *Collider Physics*. Addison Wesley, 1996.

[7] Celine Degrande, Nicolas Greiner, Wolfgang Kilian, Olivier Mattelaer, Harrison Mebane, Tim Stelzer, Scott Willenbrock, and Cen Zhang. Effective Field Theory: A Modern Approach to Anomalous Couplings. *Annals Phys.*, 335:21–32, 2013.

[8] *LHC DESIGN REPORT VOL. 1:LHC MAIN RING*, 2004.

[9] Jason Nielsen. Fundamentals of LHC Experiments. In *Proceedings, Theoretical Advanced Study Institute in Elementary Particle Physics (TASI 2010). String Theory and Its Applications: From meV to the Planck Scale: Boulder,Colorado, USA, June 1-25, 2010*, pages 127–152, 2011.

[10] E. A. Mobs. The CERN accelerator complex. `https://cds.cern.ch/record/2225847`, 2016.

[11] Lyndon Evans and Philip Bryant. LHC Machine. *JINST*, 3:S08001, 2008.

[12] World's highest energy particles (and no black hole apocalypse). `http://aviewfromtheright.com/2010/04/22/worlds-highest-energy-particle`.

[13] CMS website. `https://cms.cern/detector`.

[14] Serguei Chatrchyan et al. Description and performance of track and primary-vertex

reconstruction with the CMS tracker. *JINST*, 9(10):P10009, 2014.

[15] S. Chatrchyan et al. The CMS Experiment at the CERN LHC. *JINST*, 3:S08004, 2008.

[16] R. Paramatti. Design options for the upgrade of the CMS electromagnetic calorimeter. *Nucl. Part. Phys. Proc.*, 273-275:995–1001, 2016.

[17] A. Benaglia. The CMS ECAL performance with examples. *JINST*, 9:C02008, 2014.

[18] Hans Hofer, Jean-Louis Faure, Paul Lecoq, and Hans Rykaczewski. The electromagnetic calorimeter technical design report. Technical Report 4, CERN, December 1997.

[19] J. Mans, J. Anderson, B. Dahmes, P. de Barbaro, J. Freeman, T. Grassi, E. Hazen, R. Ruchti, I. Schimdt, et al. CMS Technical Design Report for the Phase 1 Upgrade of the Hadron Calorimeter. Technical Report 010, CMS, 2012.

[20] Tobias Hansen. *Single Hadron Response of the CMS Calorimeter*. PhD thesis, University of Hamburg, 2010.

[21] G. Cerminara. The drift tube system of the CMS experiment. *Nucl. Phys. Proc. Suppl.*, 172:71–74, 2007.

[22] M. C. Fouz. The CMS muon system. *Nucl. Instrum. Meth.*, A573:260–263, 2007.

[23] M. Abbrescia et al. The RPC system for the CMS experiment at the LHC. *Nucl. Instrum. Meth.*, A508:137–141, 2003.

[24] Vardan Khachatryan et al. The CMS trigger system. *JINST*, 12(01):P01020, 2017.

[25] Tomasz Bawej et al. The New CMS DAQ System for Run-2 of the LHC. *IEEE Trans. Nucl. Sci.*, 62(3):1099–1103, 2015. [,7097437(2014)].

[26] Kenneth Long. *Measurement of Electroweak WZ Boson Production and Search for New Physics in Proton-Proton Collisions at $\sqrt{s}$ = 13 TeV with the CMS Detector at the CERN LHC*. PhD thesis, University of Wisconsin – Madison, 2019.

[27] Vardan Khachatryan et al. Measurement of the W^+W^- cross section in pp collisions at $\sqrt{s} = 8$ TeV and limits on anomalous gauge couplings. *Eur. Phys. J.*, C76(7):401, 2016.

[28] V. Khachatryan et al. Measurement of the WZ production cross section in pp collisions

at $\sqrt{s} = 7$ and 8 TeV and search for anomalous triple gauge couplings at $\sqrt{s} = 8\,\text{TeV}$. *Eur. Phys. J.*, C77(4):236, 2017.

[29] Albert M Sirunyan et al. Search for anomalous couplings in boosted WW/WZ $\to \ell\nu\mathrm{q}\bar{\mathrm{q}}$ production in proton-proton collisions at $\sqrt{s} = 8$ TeV. *Phys. Lett.*, B772:21–42, 2017.

[30] Albert M Sirunyan et al. Search for anomalous triple gauge couplings in WW and WZ production in lepton + jet events in proton-proton collisions at $\sqrt{s} = 13$ TeV. *JHEP*, 12:062, 2019.

[31] D. Contardo, M. Klute, J. Mans, L. Silvestris, and J. Butler. Technical Proposal for the Phase-II Upgrade of the CMS Detector. 2015.

[32] A. M. Sirunyan et al. Particle-flow reconstruction and global event description with the CMS detector. *JINST*, 12(10):P10003, 2017.

[33] Vardan Khachatryan et al. Performance of Electron Reconstruction and Selection with the CMS Detector in Proton-Proton Collisions at s = 8 TeV. *JINST*, 10(06):P06005, 2015.

[34] Serguei Chatrchyan et al. Energy Calibration and Resolution of the CMS Electromagnetic Calorimeter in pp Collisions at $\sqrt{s} = 7$ TeV. *JINST*, 8:P09009, 2013. [JINST8,9009(2013)].

[35] A. M. Sirunyan et al. Performance of the CMS muon detector and muon reconstruction with proton-proton collisions at $\sqrt{s} = 13$ TeV. *JINST*, 13(06):P06015, 2018.

[36] Serguei Chatrchyan et al. Performance of CMS Muon Reconstruction in pp Collision Events at $\sqrt{s} = 7$ TeV. *JINST*, 7:P10002, 2012.

[37] Matteo Cacciari, Gavin P. Salam, and Gregory Soyez. The anti-k_t jet clustering algorithm. *JHEP*, 04:063, 2008.

[38] Daniele Bertolini, Philip Harris, Matthew Low, and Nhan Tran. Pileup Per Particle Identification. *JHEP*, 10:059, 2014.

[39] Andrew J. Larkoski, Simone Marzani, Gregory Soyez, and Jesse Thaler. Soft Drop. *JHEP*, 05:146, 2014.

[40] Jesse Thaler and Ken Van Tilburg. Identifying Boosted Objects with N-subjettiness. *JHEP*, 03:015, 2011.

[41] V. N. Aseev et al. An upper limit on electron antineutrino mass from Troitsk experiment. *Phys. Rev.*, D84:112003, 2011.

[42] K. Assamagan et al. Upper limit of the muon-neutrino mass and charged pion mass from momentum analysis of a surface muon beam. *Phys. Rev.*, D53:6065–6077, 1996.

[43] T. Stelzer and W. F. Long. Automatic generation of tree level helicity amplitudes. *Comput. Phys. Commun.*, 81:357–371, 1994.

[44] Stefano Frixione and Bryan R. Webber. Matching NLO QCD computations and parton shower simulations. *JHEP*, 06:029, 2002.

[45] Tom Melia, Paolo Nason, Raoul Rontsch, and Giulia Zanderighi. W+W-, WZ and ZZ production in the POWHEG BOX. *JHEP*, 11:078, 2011.

[46] T. Gehrmann, M. Grazzini, S. Kallweit, P. Maierhfer, A. von Manteuffel, S. Pozzorini, D. Rathlev, and L. Tancredi. W^+W^- Production at Hadron Colliders in Next to Next to Leading Order QCD. *Phys. Rev. Lett.*, 113(21):212001, 2014.

[47] Massimiliano Grazzini, Stefan Kallweit, Dirk Rathlev, and Marius Wiesemann. $W^{\pm}Z$ production at hadron colliders in NNLO QCD. *Phys. Lett.*, B761:179–183, 2016.

[48] Michal Czakon and Alexander Mitov. Top++: A Program for the Calculation of the Top-Pair Cross-Section at Hadron Colliders. *Comput. Phys. Commun.*, 185:2930, 2014.

[49] John Campbell, Keith Ellis, Walter Giele, Tobias Neumann, and Ciaran Williams. *MCFM-9.0 manual*, September 2019.

[50] Torbjorn Sjostrand, Stephen Mrenna, and Peter Z. Skands. PYTHIA 6.4 Physics and Manual. *JHEP*, 05:026, 2006.

[51] S. Agostinelli et al. GEANT4: A Simulation toolkit. *Nucl. Instrum. Meth.*, A506:250–303, 2003.

[52] Andreas Hinzmann. Search for massive resonances decaying into pairs of boosted w and z bosons at $\sqrt{s} = 13$ TeV. EXO-15-002.

[53] U. Baur and D. Zeppenfeld. Measuring the $WW\gamma$ Vertex in Single W Production at ep Colliders. *Nucl. Phys.*, B325:253–274, 1989.

[54] CMS Collaboration. CMS Luminosity Measurements for the 2016 Data Taking Period. 2017.

[55] Albert M Sirunyan et al. Measurement of the inelastic proton-proton cross section at $\sqrt{s} = 13$ TeV. *JHEP*, 07:161, 2018.

[56] Juan Rojo. PDF4LHC recommendations for Run II. *PoS*, DIS2016:018, 2016.

[57] Albert M Sirunyan et al. Search for massive resonances decaying into WW, WZ or ZZ bosons in proton-proton collisions at $\sqrt{s} = 13$ TeV. *JHEP*, 03:162, 2017.

[58] A. M. Sirunyan et al. Identification of heavy-flavour jets with the CMS detector in pp collisions at 13 TeV. *JINST*, 13(05):P05011, 2018.

[59] Vardan Khachatryan et al. Jet energy scale and resolution in the CMS experiment in pp collisions at 8 TeV. *JINST*, 12(02):P02014, 2017.

[60] CMS Collaboration. Dielectron resonance search in run 2 at s = 13 TeV pp collisions. Technical Report CMS-AN-2015/222, CMS, 2015.

[61] Reference guidelines and results for muon momentum scale and resolution in run-ii. `https://twiki.cern.ch/twiki/bin/view/CMS/MuonReferenceScaleResolRun2`.

[62] Heep electron id and isolation. `https://twiki.cern.ch/twiki/bin/view/CMS/HEEPElectronIdentificationRun2?rev=28`.

[63] Reference muon id, isolation, and trigger efficiencies for run-ii. `https://twiki.cern.ch/twiki/bin/viewauth/CMS/MuonReferenceEffsRun2`.

[64] Albert M Sirunyan et al. Performance of missing transverse momentum reconstruction in proton-proton collisions at $\sqrt{s} = 13$ TeV using the CMS detector. *JINST*, 14(07):P07004, 2019.

[65] Combine. `http://cms-analysis.github.io/HiggsAnalysis-CombinedLimit/`.

[66] S. S. Wilks. The large-sample distribution of the likelihood ratio for testing composite hypotheses. *The Annals of Mathematical Statistics*, 9(1):60–62, 1938.

[67] Vardan Khachatryan et al. Precise determination of the mass of the Higgs boson and tests of compatibility of its couplings with the standard model predictions using proton collisions at 7 and 8 TeV. *Eur. Phys. J.*, C75(5):212, 2015.

ABSTRACT

ANOMALOUS TRILINEAR GAUGE COUPLINGS AND ANGULAR VARIABLES

by

KEVIN SIEHL

May 2020

Advisor: Dr. Robert Harr

Major: Physics

Degree: Doctor of Philosophy

A study of techniques for improving limits placed on anomalous trilinear couplings of electroweak gauge bosons is presented. Electroweak gauge bosons couple to one another as well as to fermions. Deviations of these couplings from their standard model values would be a sign of new physics. Parameters that affect the couplings of the gauge bosons to each other also affect their helicity, which in turn may be measured from their decay products. Angles between the decay planes of the gauge bosons, as well as between their decay products, are measured. The analysis uses $35.9\,\mathrm{fb}^{-1}$ of proton-proton collision data from the LHC taken with the CMS detector. Building on a prior analysis that measured the fiducial cross section of $pp \to WW/WZ \to \ell\nu jj$, we show that angular variables can improve limits on anomalous couplings even further.

AUTOBIOGRAPHICAL STATEMENT

After receiving an M.S. in physics from Eastern Michigan University, I entered the Wayne State doctoral program in experimental particle physics. During my time at Wayne State, I have learned the use of statistical modeling, as well as programming in Python and C++, as well as several specialized programs. I have also worked on hardware upgrades for the Compact Muon Solenoid detector in Geneva, Switzerland. My publications include:

- Serguei Chatrchyan, et al. "Measurement of the Sum of WW and WZ Production with W+Dijet Events in pp Collisions at $\sqrt{s}$=7 TeV", *Eur.Phys.J. C73 (2013) no.2, 2283*
- M. Dragicevic, et al. "Test Beam Performance Measurements for the Phase I Upgrade of the CMS Pixel Detector", *JINST 12 (2017) no.05, P05022*